EXPERIMENTAL INVESTIGATION OF A LARGE-SCALE, TWO-DIMENSIONAL, MIXED-COMPRESSION INLET SYSTEM

Internal Performance and Drag at Transonic Conditions, M_∞=0.6 to 1.28

by Norman D. Wong and Warren E. Anderson

Ames Research Center

Moffett Field, Calif. 94035

1. Report No. NASA TN D-7445	2. Government Accession No.	3. Recipient's Catalog No.
4. Title and Subtitle **EXPERIMENTAL INVESTIGATION OF A LARGE-SCALE,** **TWO-DIMENSIONAL, MIXED-COMPRESSION INLET SYSTEM** Internal Performance and Drag at Transonic Conditions, M_∞ = 0.6 to 1.28		5. Report Date October 1973
		6. Performing Organization Code
7. Author(s) Norman D. Wong and Warren E. Anderson		8. Performing Organization Report No. A-4775
		10. Work Unit No. 501-24-05-01-00-21
9. Performing Organization Name and Address NASA Ames Research Center Moffett Field, Calif., 94035		
		11. Contract or Grant No.
		13. Type of Report and Period Covered Technical Note
12. Sponsoring Agency Name and Address National Aeronautics and Space Administration Washington, D. C., 20546		
		14. Sponsoring Agency Code

15. Supplementary Notes

16. Abstract

      A large-scale, variable-geometry inlet system with a design Mach number of 3.0 was tested at Mach numbers from 0.6 to 1.28. Variable features for off-design operation are an adjustable-height ramp system and a translating cowl. Experimental results are presented for transonic ramp and cowl positions showing the effect of throat boundary-layer bleed and vortex generators on engine-face performance. Detailed pressure and force-balance data are used to evaluate transonic drag characteristics.

17. Key Words (Suggested by Author(s)) Airbreathing inlets Total-pressure recovery Boundary-layer-bleed systems Vortex generators Inlet drag	18. Distribution Statement Unclassified -- Unlimited		
19. Security Classif. (of this report) Unclassified	20. Security Classif. (of this page) Unclassified	21. No. of Pages 45	22. Price* Domestic, $3.00 Foreign, $5.50

NOTATION

A area

A_c capture area (196 in.^{2} (1264.5 cm^2)), defined at $\alpha = 0°$

A_r frontal area of ramp surface

A_t throat area

C_D drag coefficient, $\dfrac{D}{q_\infty A_c}$

C_F average skin-friction coefficient

D drag

D_a additive drag

D_{cs} drag on compression surface

D_{ext} external drag

D_f friction drag

D_i internal drag

D_m model drag

D_{p_1} pressure drag at the inlet lip

D_{sp} spillage drag

h height

h_t throat height

M Mach number

m mass flow

m_∞ capture mass flow, $\rho_\infty V_\infty A_c$

$\dfrac{m_1}{m_\infty}$ inlet mass-flow ratio

$\dfrac{m_{bl}}{m_\infty}$ boundary-layer bleed mass-flow ratio

p	static pressure
$\dfrac{p}{p_\infty}$	static-pressure ratio
p_t	total pressure
$\bar{p}_{t_2}$	area weighted average total pressure at engine-face station
$\bar{p}_{t_{bl}}$	area weighted average total pressure at bleed-duct station
$\dfrac{\bar{p}_{t_2}}{p_{t_\infty}}$	main-duct total-pressure recovery ratio
Δp_{t_2}	distortion index, $\dfrac{p_{t_2\max} - \bar{p}_{t_2\min}}{\bar{p}_{t_2}}$, at engine-face station
q	dynamic pressure, $\dfrac{1}{2}\rho V^2$
R_x	Reynolds number based on local flow conditions and distance x from leading edge, $\dfrac{\rho V x}{\mu}$
V	velocity
$\dfrac{V_l}{V_o}$	boundary-layer local velocity ratio (referenced to velocity at $h = 1.0$ in. (2.54 cm))
α	angle of attack, deg
β	angle of yaw, deg
δ_1	deflection of ramp 1 from free stream at $\alpha = 0°$, deg
δ_2	deflection of ramp 2 from free stream at $\alpha = 0°$, deg
ρ	mass density
μ	viscosity from Sutherland's formula in which the local static temperature is used
$\overline{(\ )}$	average value

Subscripts

∞	free stream
0	ramp leading-edge station
1	inlet lip station

iv

2	engine-face station
b	inlet base
bal	balance
bl	bleed
e	inlet exit station
l	local
r	ramp surface

EXPERIMENTAL INVESTIGATION OF A LARGE-SCALE, TWO-DIMENSIONAL, MIXED-COMPRESSION INLET SYSTEM

Internal Performance and Drag at
Transonic Conditions, $M_\infty = 0.6$ to 1.28

Norman D. Wong and Warren E. Anderson

Ames Research Center

SUMMARY

A two-dimensional, mixed-compression, variable-geometry inlet model with a design Mach number of 3.0 has been tested at transonic Mach numbers of 0.6 to 1.28 for which the unit Reynolds number varied from 3.4×10^6 to 4.3×10^6 per foot (11.2×10^6 to 14.1×10^6 per meter), respectively.

Design point performance at $M_\infty = 3.0$ and performance of a selected configuration over the off-design supersonic Mach number range of 1.55 to 3.2 have already been reported. The present report covers the effects on engine-face total pressure performance of throat boundary-layer bleed and vortex generators for transonic ramp and cowl positions. Transonic inlet drag characteristics are evaluated from detailed pressure and force-balance measurements.

INTRODUCTION

Inlet systems designed for high performance at supersonic conditions are often required to operate efficiently at transonic speeds. For example, advanced aircraft are invariably required to cruise efficiently at near-sonic flight speeds; also, supersonic cruise vehicles operate with minimum thrust minus drag at low supersonic speeds.

A two-dimensional inlet system designed for optimum performance at a Mach number of 3.0 has been studied in detail, analytically and experimentally, at Ames Research Center. The inlet system is a mixed-compression, variable-geometry type that uses a boundary-layer bleed system and a variable-height ramp system. A translatable cowl is moved rearward from the design position to obtain high compression efficiency and low external drag at low supersonic, transonic, and subsonic flight Mach numbers.

The inlet model was tested in the Ames Unitary Plan Wind Tunnels at $M_\infty = 0.6$ to 3.2. Inlet performance showing the effects of a wide range of geometric and aerodynamic variables has been reported for a Mach number range of 1.55 to 3.2 in references 1 and 2. Internal performance and drag are reported here for Mach numbers from 0.6 to 1.28. The unit Reynolds number varied from 3.4×10^6 per foot (11.2×10^6 per meter) at $M_\infty = 0.6$ to 4.3×10^6 per foot (14.1×10^6 per meter) at $M_\infty = 1.28$.

MODEL, APPARATUS, AND TEST PROCEDURE

A detailed description of the two-dimensional inlet research model, apparatus, and test procedure is presented in reference 1. Figure 1 is a photograph of the model; figure 2 is a detailed drawing. Pertinent features of the model are: an adjustable ramp assembly and a translatable cowl to provide optimum performance at off-design and a fixed conical exit plug with a translating sleeve to control main duct flow. Throat region boundary-layer bleed was controlled by a variable area exit plug. The model was mounted on a six-component force balance for measuring inlet drag.

The relationship of second-ramp angle to throat height and area ratio is shown in figure 3. It was indicated in reference 2 that the throat height was essentially fixed near the maximum value for Mach numbers of 2.0 and below. The effect of slight throat-height variations below the maximum (shaded region in fig. 3) was investigated at transonic speeds. Variations in diffuser area ratio are presented in figure 4 for several representative second-ramp angles. Area A is the local area in a plane normal to the duct center line. The cowl was normally retracted to the aft position for transonic operations; however, the effects of small forward movement of the cowl were investigated. Design coordinates for $\delta_2 = 14°$ are presented in table 1, which also includes fillet radii for a transition from the rectangular throat to an oval shape at the engine-face station.

The details of the boundary-layer bleed system, vortex generators, and pressure rakes are presented in figure 5. The bleed plate configuration is essentially the same as that contained in references 1 and 2 (configuration 80VRF). However, when the inlet was operated at transonic conditions, boundary-layer bleed flow was controlled differently from that at higher Mach numbers. No bleed was provided in bleed zones I and II to preclude the possibility of reverse flow through the bleed-plate holes. This was accomplished by sealing the bleed zone exits with cover plates. As shown in figure 5, with full retraction of the cowl, only plate C1 (a blank plate) and about half of plate C2 were exposed to the air flow. Since the bleed through plate C2 would be negligible, it was also blanked off. Therefore, there was no cowl bleed during transonic operation. As a result, boundary-layer bleed was provided only on the ramp and side-wall surfaces in the throat region (bleed zone III) of the duct.[1] The bleed passed through perforated plates (ramp R4 and side wall S4) and was exhausted through bleed duct 3. The plate perforations were as follows:

	Ramp plate R4	Side-wall plate S4
Hole diameter, in. (cm)	0.078 (0.198)	0.125 (0.318)
Porosity, percent	7.6	13

Retaining the bleed plate configurations of bleed zones I and II (but closing the bleed exits) provides a simulation of the internal geometry and boundary-layer control for practical off-design transonic operation.

Flush static-pressure orifices were located along the mid-duct line of all four internal surfaces and the external surfaces in the leading-edge region of the cowl and side walls. Boundary-layer rakes

---

[1] The original bleed configuration required that plates R5, R6, S5, and S6 be blank.

were located at three stations on the ramp and at one station on both the cowl and right side wall. A static-pressure rake was located at the lip leading-edge station. The measurements of inlet static pressure from this rake and from surface statics on the ramp and side-wall surfaces were used in computing inlet additive drag (see Appendix). A strain-gage-type, six-component force balance was used to obtain inlet external drag values. During the external drag portion of the investigation, the exit plug assembly was removed and three fixed isentropic-flow axisymmetric convergent nozzles were successively installed at the main exit. Instrumentation on the nozzles included exit and base static-pressure orifices to provide necessary data for determining internal and base drag corrections to the balance drag measurements. The inlet external drag coefficient was obtained as described in the Appendix.

Bleed mass-flow ratio and total-pressure recovery were determined from rake measurements of static and total pressure near the exit of the bleed duct. Total-pressure measurements from the engine-face rakes were area weighted to determine main-duct total-pressure recovery. The average recovery was then used, together with the average engine-face static pressure, to calculate the main-duct mass-flow ratio.

RESULTS AND DISCUSSION

Inlet Compression Efficiency

Engine-face performance— The basic inlet transonic compression efficiency performance is plotted in figure 6. Engine-face total-pressure-recovery ratio and distortion index are plotted against inlet mass-flow ratio for free-stream Mach numbers from 0.6 to 1.28. Angle of attack and angle of yaw were fixed at $0°$, and the throat height was set at the maximum value which corresponded to $\delta_2 = 6°$. The internal porous plate configuration provided boundary-layer bleed only on the throat ramp and side-wall surfaces. Vortex generators were installed and the cowl was fully retracted to model station 52 (132.08) for these data and all subsequent data unless otherwise noted. At the lower Mach numbers, the total-pressure recovery decreases as the mass-flow ratio approaches the maximum value attainable. This effect is characteristic of subsonic inlet performance where friction losses increase rapidly as inlet velocities approach sonic conditions. Friction and shock-wave losses account for the decrease in maximum recovery values with increasing free-stream Mach numbers up to the highest test value, $M_\infty = 1.28$. In addition, the distortion index increased as mass flow or Mach number increased. A substantial drop in recovery is indicated at reduced mass-flow ratios for supersonic free-stream Mach numbers, although the distortion index remains essentially constant. This can be attributed to the adverse pressure gradients on the ramp surface forward of the cowl lip. These gradients are increased with increased spillage (reduced mass-flow ratio), which results in boundary-layer separation. Flow separation is indicated by ramp boundary-layer profile measurements (discussed in subsequent paragraphs). Both the adverse gradients and flow separation were more severe at supersonic Mach numbers than at subsonic Mach numbers, possibly due to the presence of shock waves on the ramp surface. The result is a reduction in engine-face recovery with decreasing mass-flow ratio. Throat boundary-layer bleed provided for an increase in recovery and a decrease in distortion (except for high mass-flow ratios at $M_\infty = 0.6$); however, the characteristic trends of these parameters with mass-flow ratio were not affected.

3

A detailed evaluation of engine-face total-pressure performance at $M_\infty = 1.28$ is presented in figures 7 and 8. Local total-pressure ratio contours (fig. 7) show the effects of throat bleed at maximum and minimum recovery (low mass-flow ratio). The bleed mass-flow ratio at $M_\infty = 1.28$ is about 0.025 and bleed is effective in removing part of the low-energy flow from the ramp side of the inlet duct. The adverse effect on recovery of reducing the mass-flow ratio is revealed to be due primarily to a general reduction in the local total-pressure ratio and reduced high-energy core flow. This result is due to incomplete mixing of the entering separated boundary layer within the subsonic diffuser. Further evidence of the effects of boundary-layer bleed and inlet mass flow on engine-face performance is shown by the vertical total-pressure profiles in figure 8. Low total pressure prevails on the ramp side of the duct because the ramp curvature and adverse pressure gradient inhibit complete flow mixing across the full height of the duct. The profiles are improved by throat bleed, but the upstream separation present at reduced mass-flow ratios has an adverse effect, although flow separation does not appear to persist to the engine-face station. These profiles also explain the high levels of distortion index indicated for $M_\infty = 1.28$ in figure 6. Large viscous effects are present at the engine face and hence large total pressure losses occur near the duct wall. The result is high distortion, even under maximum recovery conditions when the flow is well mixed throughout the duct.

The effects of inlet geometric variations on engine-face performance are shown in figures 9 and 10 for $M_\infty = 1.28$. Both maximum recovery and distortion were improved slightly by the use of vortex generators that provide forced mixing in the subsonic diffuser (fig. 9). Figure 10 shows the effects of cowl position and throat height (change in δ_2) on engine-face performance. A forward cowl movement of 4 in. (10.2 cm) reduces the maximum recovery slightly, with a corresponding increase in distortion and a slight increase in maximum inlet mass-flow ratio. Decreasing the throat height to correspond to $\delta_2 = 7°$ produced the expected decrease in maximum mass-flow ratio, but no appreciable change is indicated in maximum recovery.

The effects of angle of attack and yaw on engine-face performance at $M_\infty = 1.28$ is presented in figure 11. Increasing the angle of attack increases the recovery at reduced mass-flow ratios. Ramp static-pressure distributions (not shown) indicate that the additional turning of the flow at higher angle of attack causes increased static pressures on the ramp surface in the vicinity of the cowl lip. As a result, boundary-layer bleed was increased at the lower mass-flow ratios, which improved recovery. Angle of yaw had no effect within the range tested.

Bleed-system performance— The bleed-system performance is shown in figure 12 for the maximum bleed exit area. Boundary-layer bleed mass-flow ratio and bleed-duct total-pressure-recovery ratio are plotted against inlet mass-flow ratio for free-stream Mach numbers from 0.6 to 1.28. The bleed mass-flow ratio is affected by the bleed system pumping capability, which is indicated by the relative level of the bleed-duct total pressure and the free-stream static pressure. Bleed-duct total pressure also indicates the level of ramp static pressure approaching the porous bleed surfaces. At the high Mach numbers, the bleed mass-flow ratio remains relatively constant in the 0.02 to 0.03 range because the bleed-duct total pressure (and consequently the ramp static pressure) is sufficiently greater than free-stream static pressure to provide the necessary pumping requirements. At low Mach numbers, no bleed is indicated at a high mass-flow ratio because duct total pressure is about equal to free-stream static pressure, indicating low static-pressure ratios on the ramp. Reverse flow is possible for those data points where free-stream static pressure is greater than the bleed-duct total pressure. This could explain the adverse effect of bleed for the maximum mass-flow ratio point at $M_\infty = 0.6$ (fig. 6). Bleed increases as mass flow decreases because the spillage is associated with

4

increased ramp static pressure which increases pumping action. It is evident that bleed discharge can be a problem at subsonic and low transonic speeds because of the limited pumping capability.

Boundary-layer characteristics— Boundary-layer profiles of total-pressure ratio, Mach number, and velocity ratio are presented in figures 13, 14, and 15, respectively. The profiles are presented for the maximum test Mach number, 1.28, and for 0.85, which is a nominal vehicle subsonic cruise condition. In figure 13, upstream profiles were measured on the ramp forward of the bleed region (lip station). Throat measurements were made immediately downstream of the bleed region on the ramp and side wall but further downstream on the unbled cowl surface. Downstream profiles were measured on the forward portion of ramp 4 (see fig. 5). The upstream and throat measurements for $M_\infty = 1.28$ (fig. 13(a)) indicate low-energy profiles on the ramp surface at high mass-flow ratios and separated profiles at low mass-flow ratios indicated by equal values of total and static pressure near the surface. Downstream profiles show uniform, well-developed flow, except that separation is indicated for minimum mass-flow ratio; however, figure 8 indicates no separation present at the engine-face station. For maximum engine-face recovery (0.952), high-energy boundary layers existed on the cowl and side-wall surfaces at the throat station. A boundary-layer thickness of about 0.25 in. (0.635 cm) is indicated on the cowl, whereas the corresponding side-wall thickness is minimal. Figure 13(b) exhibits higher boundary-layer energy levels for $M_\infty = 0.85$ than was the case for $M_\infty = 1.28$. However, the profiles for lowest mass-flow ratios at the upstream and throat locations again suggest possible flow separation on the ramp surface.

Throat total-pressure profiles are converted to local Mach number profiles in figure 14. The profiles are considered qualitative in nature because of the uncertainty in the measurement of static pressure with the throat rake, which was provided with a single static tube (fig. 5). A maximum core-flow Mach number of about 0.85 is indicated at both $M_\infty = 1.28$ and 0.85 for the maximum mass-flow ratio. As noted earlier, operating at the lowest mass-flow ratio resulted in separated ramp flow (dashed curves); however, core-flow Mach numbers remained high as indicated by the cowl and side-wall profiles.

Boundary-layer velocity profiles for the downstream ramp station are presented in figure 15. At high mass-flow ratios, the forced mixing action of vortex generators is evident at both $M_\infty = 1.28$ and 0.85 (vortex generators are shown to be beneficial to engine-face distortion in fig. 9). At a minimum mass-flow ratio, the separated flow on the ramp surface at the throat persists to the downstream station (see fig. 13); therefore, static and total pressures are essentially equal and no significance can be attached to the downstream velocity profiles (dashed curves) because of measurement inaccuracies.

Inlet Drag

Inlets designed for supersonic speeds are generally operated at substantially reduced mass-flow ratios at transonic speeds. Excess air, spilled forward of the inlet cowl surfaces, produces relatively large values of inlet spillage drag. Spillage drag together with other possible inlet drag components, bleed and bypass drag, affect vehicle transonic cruise performance. Also, inlet drag is a major factor in fixing engine size to meet vehicle transonic acceleration requirements. Transonic spillage drag is evaluated in reference 3, and two significant inlet drag studies are discussed in references 4 and 5.

In the present study, inlet external drag is considered to consist of a true model external drag plus additive drag. Additive drag is a corrective force made necessary by the standard definition for net thrust[2] and can be a large contributor to inlet external drag. The spillage drag component of inlet external drag is usually less than the additive drag because of favorable cowl-lip suction effects resulting from inlet operation at less than the reference mass-flow ratio condition. For an operational aircraft, the spillage drag would include the change in all interference effects on vehicle surfaces affected by the inlet flow field. The mathematical development for determining inlet external drag and related drag components, spillage and additive drag, used during the present study is contained in the Appendix.

The measured transonic additive drag performance of the two-dimensional inlet research model is shown in figure 16. The curves show additive drag coefficient increases with both decreasing mass-flow ratio and increasing free-stream Mach number (except from $M_\infty = 1.15$ to 1.28). Throat bleed does not appreciably affect additive drag levels except at $M_\infty = 0.60$.

Reference 4 presents a theoretical procedure for calculating additive drag based on inviscid one-dimensional continuity of mass relationships. Figure 17 shows a comparison of theoretical and experimental additive drag coefficient at $M_\infty = 1.28$ and 0.60. The basic theory overpredicts the additive drag at $M_\infty = 1.28$ by more than threefold and also shows substantial disagreement with experiment at $M_\infty = 0.60$. A major discrepancy between inviscid theory and experiment involved the ramp drag term in the additive drag equation. Ramp drag was determined from static-pressure distributions on the ramp surface and figure 18 shows large differences between theoretical and experimental ramp static-pressure values. The theoretical distributions were determined by using a linear variation between the initial ramp station and the inlet lip station. Static pressure at the initial ramp station was taken as the value behind a detached normal-shock wave for $M_\infty = 1.28$ and as the free-stream value for $M_\infty = 0.60$. Lip station static pressure was determined from the continuity of mass relationships together with assumptions of normal-shock-wave recovery and free-stream recovery at $M_\infty = 1.28$ and 0.60, respectively. The experimental static pressures were generally much lower than the theoretical predictions except for the maximum mass-flow ratio at $M_\infty = 0.60$. For both Mach numbers, the experimental pressures indicate that the ramp flow expanded after an initial pressure rise at the leading edge and remained at a minimum until compression was realized ahead of the cowl due to spillage. More sophisticated theoretical methods are needed to predict pressures on the forward ramp surface. At $M_\infty = 1.28$, supersonic flow is indicated by the lowest pressures on the ramp surface, suggesting shock waves were present downstream which contributed to the separated flow at reduced mass-flow ratios. Such complicated viscous ramp flows, which obviously were not approximated by inviscid one-dimensional theory, had the effect of increasing inlet Mach number and thus producing static pressure values much lower than predicted. The theoretical discrepancies due to ramp drag (fig. 17) were obtained by substituting experimental ramp drag values for theoretical values in the theoretical computations. The remaining theoretical discrepancies were due to the total pressure profiles at the inlet station which affected the stream thrust terms in the additive drag equation.

The experimental additive drag coefficients were subject to some error because of incomplete pressure instrumentation at the inlet station. Average static pressure measurements were used to calculate an average velocity ($\bar{V}_1$). The true effects of a velocity profile are not accounted for by such an averaging method since total-pressure and static-pressure measurements are required to

---

[2] Net thrust is the gross thrust at the exhaust plane minus the free-stream ram drag.

properly assess velocity profile effects in a momentum balance. Approximate corrections to $\overline{V}_1$ were made based on boundary-layer rake total-pressure measurements and the qualitative uncertainties in the experimental data are indicated by the shaded regions in figure 17.

A comparison of the theoretical and experimental minimum additive drag coefficient occurring at maximum mass-flow ratio is shown in figure 19 for a range of experimental Mach numbers. Good agreement is shown at Mach numbers less than 1.0 if theory is adjusted for experimental ramp drag only. For supersonic Mach numbers, the added adjustment for inlet profile was also necessary to obtain reasonable agreement.

Experimental inlet drag is analyzed further in figure 20. The data are shown for $M_\infty = 1.28$, which is representative of the trend in inlet drag over the full range of transonic test Mach numbers. Additive drag increased with forward movement of the cowl; the largest effect occurred between cowl-lip positions 52 (132.1) and 50 (127.0) at maximum mass-flow ratio. The increases are consistent with the general rule that increasing inlet area reduces inlet Mach number and increases inlet additive drag. In a final optimization study of cowl position, the drag penalties would be traded off against possible advantages in engine-face total-pressure recovery (fig. 10).

Three exit nozzle sizes were used in measuring external drag at three mass-flow ratio conditions. Note that the absolute level of external drag coefficient (fig. 20) is not significant but rather the shape (slope) of the external drag curve indicates the change in spillage drag with mass-flow ratio (see Appendix).

As a measure of the cancellation effects of cowl forces on the additive drag, an additive drag correction factor termed K_{ADD} was introduced in reference 4. The term K_{ADD} is the change in external drag from a given reference mass-flow ratio divided by the corresponding change in experimental additive drag.[3] Hence, $K_{ADD} < 1.0$ indicates cowl suction. The qualitative characteristics of K_{ADD} are shown in figure 21 for three representative transonic Mach numbers. The error bands shown indicate the uncertainties involved in measuring both additive and external drag. The trends shown indicate significant cowl suction at $M_\infty = 1.00$ and 1.28 for the full range of mass-flow ratio. For $M_\infty = 0.6$, cowl suction effects are evident only at reduced mass-flow ratio. The ramp pressure distributions (fig. 18) can be used to explain these local cowl lip characteristics. Local ramp pressure was increased in the region of the cowl-lip station at all mass-flow ratios for $M_\infty = 1.28$ and at reduced mass-flow ratios for $M_\infty = 0.6$. These pressure increases indicate flow spillage and therefore increasing flow angularity at the cowl lip. Flow angularity, in turn, should increase the flow expansion over the external lip surface, producing favorable negative pressures.

CONCLUDING REMARKS

The results of an experimental investigation of a two-dimensional, mixed-compression inlet system with a design Mach number of 3.0 have been presented for Mach numbers from 0.6 to 1.28. A variable ramp system and a translating cowl were used for off-design operation. Boundary-layer bleed was provided in the throat region on the ramp and side-wall surfaces. Maximum total-pressure recovery at the engine-face station varied from about 0.95 at $M_\infty = 1.28$ to about 0.99 at

---

[3] Reference 4 uses theoretical additive drag in the K_{ADD} relationship.

$M_\infty = 0.6$. The boundary-layer bleed mass-flow ratio at $M_\infty = 1.28$ was about 0.025, and eliminating bleed reduced the maximum recovery to 0.93. Performance was insensitive to variations in angle of attack and angle of yaw to $4°$, and vortex generators that proved advantageous at design speeds were not significantly effective at transonic speeds.

Inlet drag characteristics were determined from detailed pressure and force-balance measurements. One-dimensional inviscid theory is inadequate for predicting additive drag, primarily because of large viscous effects on the ramp surface. As a result, the inviscid theory does not adequately predict the ramp pressure distribution or the inlet flow distribution at the lip station.

Ames Research Center
National Aeronautics and Space Administration
Moffett Field, Calif., 94035, April 24, 1973

8

APPENDIX

INLET DRAG

Inlet Additive Drag

The additive drag expression is derived from a force-momentum balance of the stream-tube element shown in sketch (a). The drag forces in the axial direction acting on the element
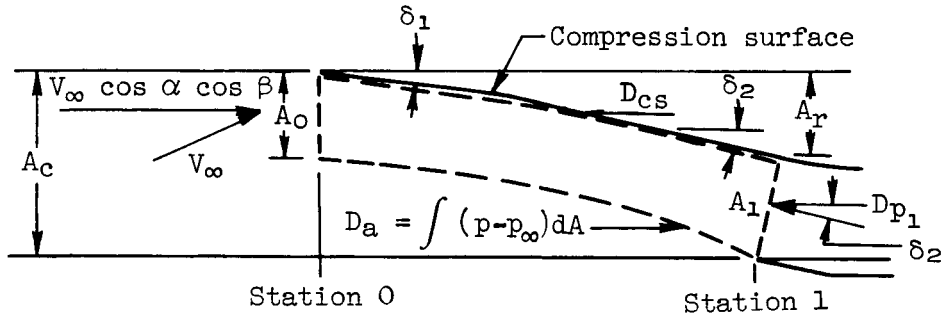
Sketch (a)

(unbounded stream tube) are equal to the momentum change in the axial direction. Thus, for positive α and β, which are referred to a thrust axis,

$$D_a - D_{p_1} - D_{cs} = m_1 (\bar{V}_1 \cos \delta_2 - V_\infty \cos \alpha \cos \beta)$$

and

$$D_a = m_1 (\bar{V}_1 \cos \delta_2 - V_\infty \cos \alpha \cos \beta) + D_{p_1} + D_{cs}$$

The element pressure drag at the inlet lip, D_{p_1}, is:

$$D_{p_1} = \int (p_1 - p_\infty) dA_1 \cos \delta_2$$

The term D_{cs} is defined as the drag on the compression surface which includes that due to pressure and friction (on the ramp and side-wall surfaces):

$$D_{cs} = \int (p_r - p_\infty) dA_r + D_f$$

Substituting terms and writing in coefficient form

$$C_{D_a} = 2 \frac{m_1}{m_\infty} \left(\frac{\bar{V}_1}{V_\infty} \cos \delta_2 - \cos \alpha \cos \beta \right) + \int \frac{p_1 - p_\infty}{q_\infty A_c} dA_1 \cos \delta_2 + \int \frac{p_r - p_\infty}{q_\infty A_c} dA_r + C_{D_f}$$

The experimental evaluation of the additive drag coefficient involved measuring the static pressures and areas necessary for all terms except velocity ratio, $\bar{V}_1 / V_\infty$. The calculated average value of V_1 is obtained using continuity relationships to obtain $\bar{M}_1$ and then solving for

9

$$\frac{\overline{V}_1}{V_\infty} = \frac{\overline{M}_1 (1 + 0.2M_\infty^2)^{1/2}}{M_\infty(1 + 0.2\overline{M}_1^2)^{1/2}}$$

The skin-friction drag coefficient is defined as

$$C_{D_f} = \frac{D_f}{q_\infty A_c} = \frac{C_F q A}{q_\infty A_c} = \frac{C_F \overline{p} M^2 A}{p_\infty M_\infty^2 A_c}$$

in which $\overline{p}$ is the average local pressure over the wetted surface area, A, and C_F is defined by the Prandtl-Schlichting approximate formula for average skin-friction coefficient as

$$C_F = \frac{0.455(1 + 0.2M^2)^{-0.467}}{(\log R_x)^{2.58}}$$

The Mach number was arbitrarily defined for this test as the average Mach number within the stream tube

$$M = \frac{1}{2}(M_0 + \overline{M}_1)$$

Inlet External Drag

The inlet external drag can be expressed as

$$D_{ext} = D_{bal} - D_b - D_i$$

where

D_{bal} balance drag measurement

D_b base drag, $\int (p_\infty - p_b)dA_b$

D_i internal drag, $m_1 (V_\infty \cos \alpha \cos \beta - \overline{V}_e) + \int (p_\infty - p_e)dA_e^1$
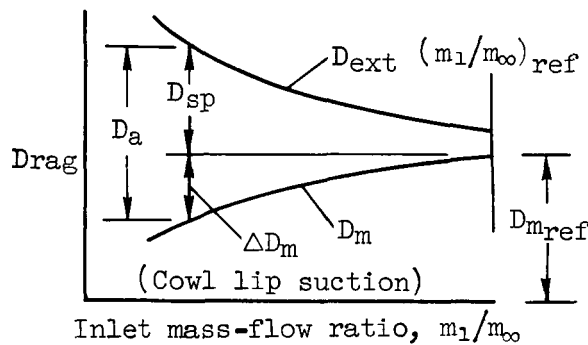
Sketch (b)

Substituting terms and writing in coefficient form, one obtains

$$C_{D_{ext}} = C_{D_{bal}} - C_{D_b} - 2\frac{m_1}{m_\infty}\left(\cos \alpha \cos \beta - \frac{\overline{V}_e}{V_\infty}\right) - \int \frac{p_\infty - p_e}{q_\infty A_c} dA_e$$

The relationship of additive drag to external drag is represented by sketch (b). External drag is defined as the sum of the model drag (true external model drag corrected for base pressure drag) and the additive drag

---

[1]This equation is for the no boundary-layer bleed condition. When bleed exists, the portion of internal drag due to bleed must also be evaluated.

$$D_{ext} = D_m + D_a$$

Spillage drag is a term indicating the increase in external drag above the reference model drag, $D_{m_{ref}}$, which exists at a specified reference mass-flow ratio, $(m_1/m_\infty)_{ref}$,

$$D_{sp} = D_a - \Delta D_m$$

REFERENCES

1. Anderson, Warren E.; and Wong, Norman D.: Experimental Investigation of a Large-Scale, Two-Dimensional, Mixed-Compression Inlet System-Performance at Design Conditions, $M_\infty = 3.0$. NASA TM X-2016, 1970.

2. Wong, Norman D.; and Anderson, W. E.: Experimental Investigation of a Large-Scale, Two-Dimensional, Mixed-Compression Inlet System-Performance at Supersonic Conditions, $M_\infty = 1.55$ to 3.2. NASA TN D-6392, 1971.

3. Anderson, W. E.; Petersen, Martine W.; and Sorensen, Norman E.: An Evaluation of Transonic Spillage Drag Based on Test Results from Large-Scale Inlet Models. NASA SP-124, 1966, pp. 171-184.

4. Petersen, Martine W.; and Tamplin, Gordon C.: Experimental Review of Transonic Spillage Drag of Rectangular Inlets. AFAPL-TR-66-30, North American Aviation, Inc., 1966.

5. McVey, F. D.; Rejeske, J. V.; Phillips, E. J.; et al.: Experimental Evaluation of Inlet Drag Characteristics in the Transonic Mach Number Regime. AFAPL-TR-68-119, McDonnel-Douglas Corp., 1968.

12

TABLE 1.– DESIGN COORDINATES, $\delta_2 = 14°$

Model station		Height station				Duct height		Duct width		Fillet radius			
		Ramp surface		Cowl surface						Ramp surface		Cowl surface	
in.	cm	in.	cm	in.	cm	in.	cm	in.	cm	in.	cm	in.	cm
0	0	0	0					14.00	35.56				
		*	*										
28.00	71.12	3.438	8.733										
30.40	77.22	*	*	14.00	35.56								
54.14	137.52	9.954	25.283										
55.00	139.70	10.158	25.801										
56.00	142.24	10.367	26.332										
57.00	144.78	10.533	26.754										
58.00	147.32	10.615	26.962										
58.80	149.35	10.645	27.038			3.355	8.522						
60.28	153.11					3.355	8.522						
61.76	156.87					3.368	8.555						
63.24	160.63					3.394	8.621						
64.72	164.39					3.432	8.717						
65.52	166.42	10.544	26.782			3.456	8.778						
66.50	168.91					3.482	8.844						
67.85	172.34					3.535	8.979						
69.52	176.58					3.632	9.225						
71.12	180.64					3.763	9.558						
72.00	182.88	10.147	25.773	*	*	3.853	9.787						
73.74	187.30			*	*	3.92	9.96						
74.50	189.23			13.80	35.05	*	*					0	0
77.62	197.15					4.31	10.95					.29	.74
80.00	203.20	9.19	23.34			4.61	11.71					.56	1.42
81.52	207.06					4.82	12.24			0	0	.76	1.93
82.50	209.55					4.97	12.62			.15	.38	.91	2.31
85.00	215.90	8.40	21.34			5.40	13.72			.58	1.47	1.29	3.28
87.50	222.25					5.89	14.96			1.09	2.77	1.80	4.57
90.00	228.60	7.36	18.69			6.44	16.36			1.62	4.11	2.39	6.07
92.50	234.95					7.04	17.88			2.22	5.64	2.92	7.42
95.52	242.62	5.94	15.09			7.86	19.96			3.04	7.72	3.50	8.89
97.50	247.65					8.40	21.34			3.58	9.09	3.84	9.75
99.33	252.30					8.86	22.50			4.03	10.24	4.11	10.44
101.36	257.45	4.52	11.48	13.86	35.20	9.34	23.72			4.48	11.38	4.38	11.13
102.50	260.35			13.91	35.33	9.59	24.36			4.69	11.91	4.53	11.51
105.00	266.70	3.92	9.96	14.08	35.76	10.16	25.81	*	*	5.08	12.90	4.91	12.47
107.28	272.49			14.38	36.53	10.76	27.33			5.38	13.66	5.38	13.67
110.00	279.40	3.26	8.28	*	*	11.48	29.16			5.74	14.58	5.74	14.58
113.02	287.07					12.28	31.19	12.80	32.51	6.14	15.60	6.14	15.60
115.02	292.15	2.60	6.60	15.40	39.12	12.80	32.51	12.80	32.51	6.40	16.26	6.40	16.26

*Straight line between points
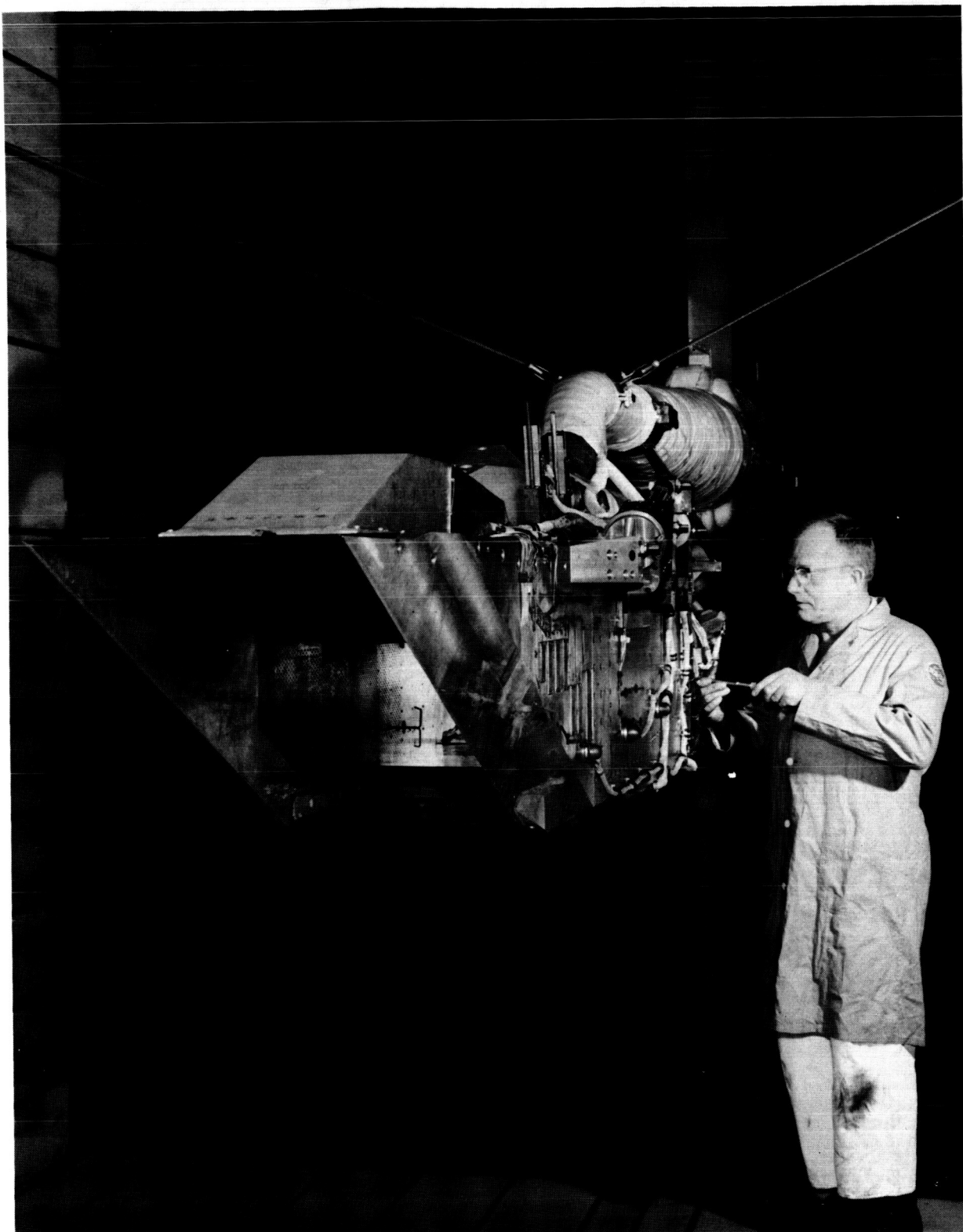
Figure 1.- The two-dimensional inlet research model installed in the Ames
11-by 11-Foot Unitary Plan Wind Tunnel.

Figure 2.- A drawing of the two-dimensional inlet research model; $\delta_2 = 7°$, cowl fully retracted.

16
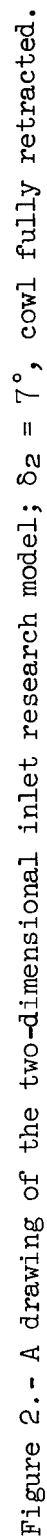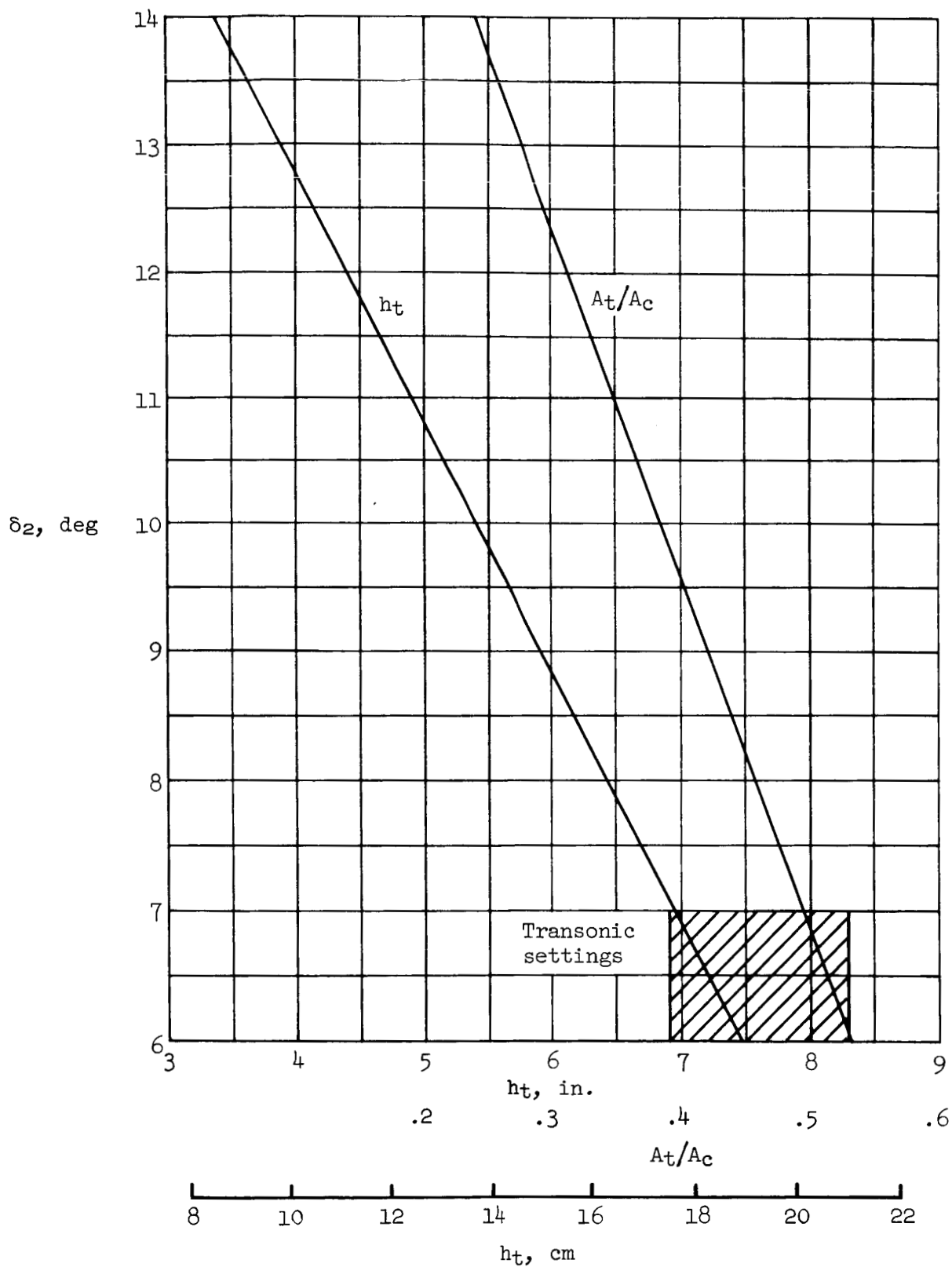
Figure 3.- Relationship of second-ramp angle to throat height and area ratio.
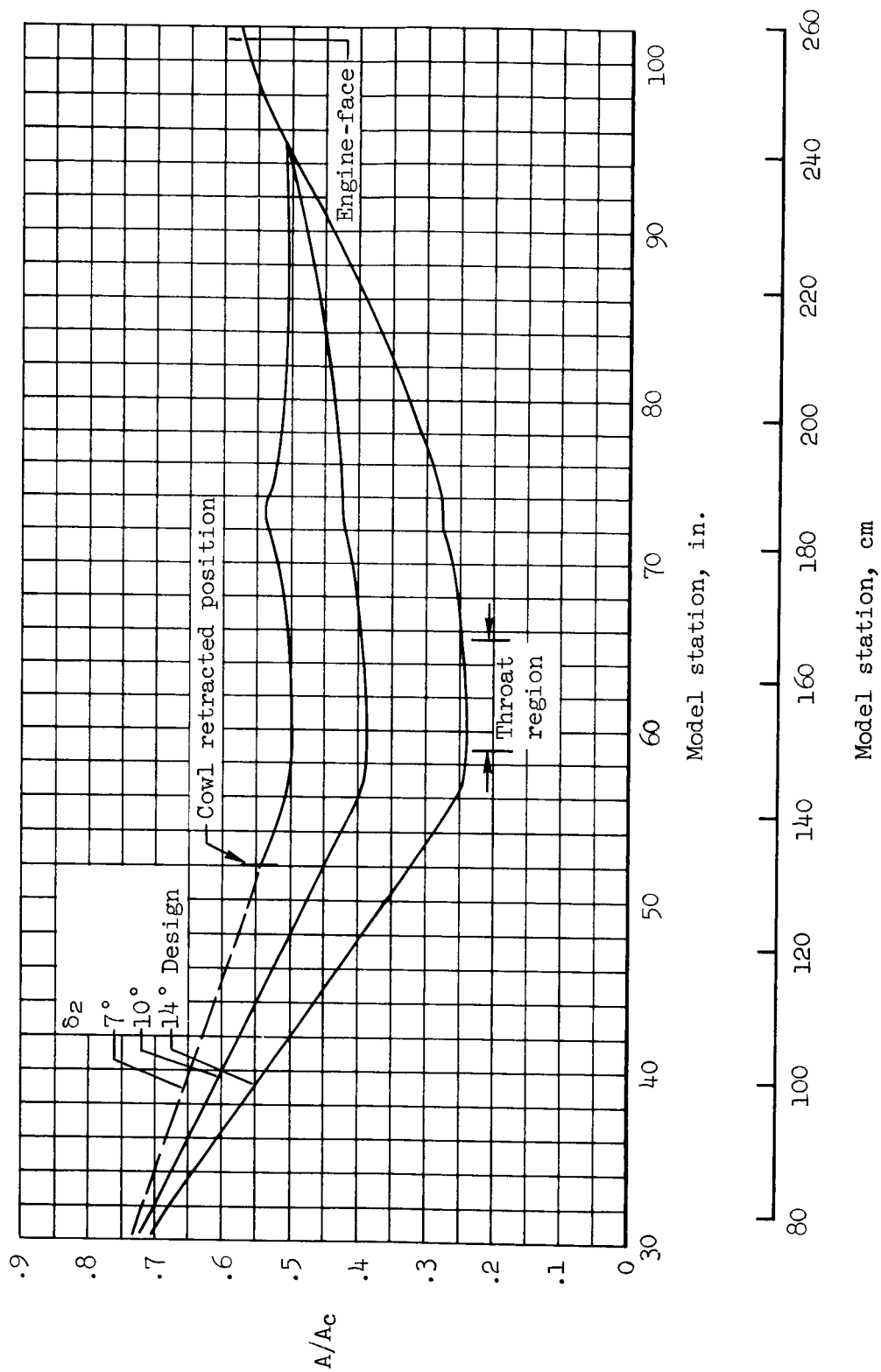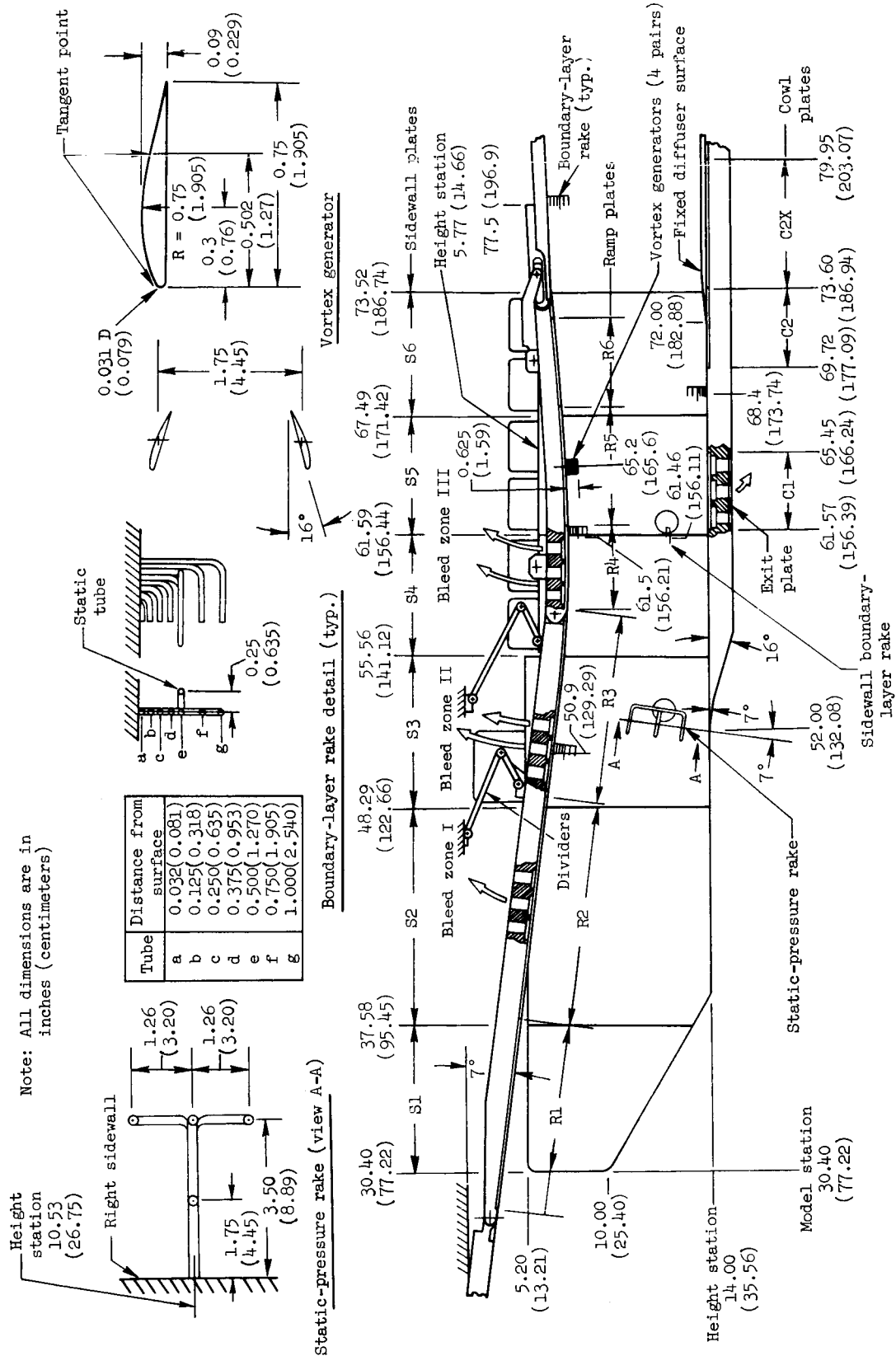
Figure 4.- Diffuser area-ratio variation.

18

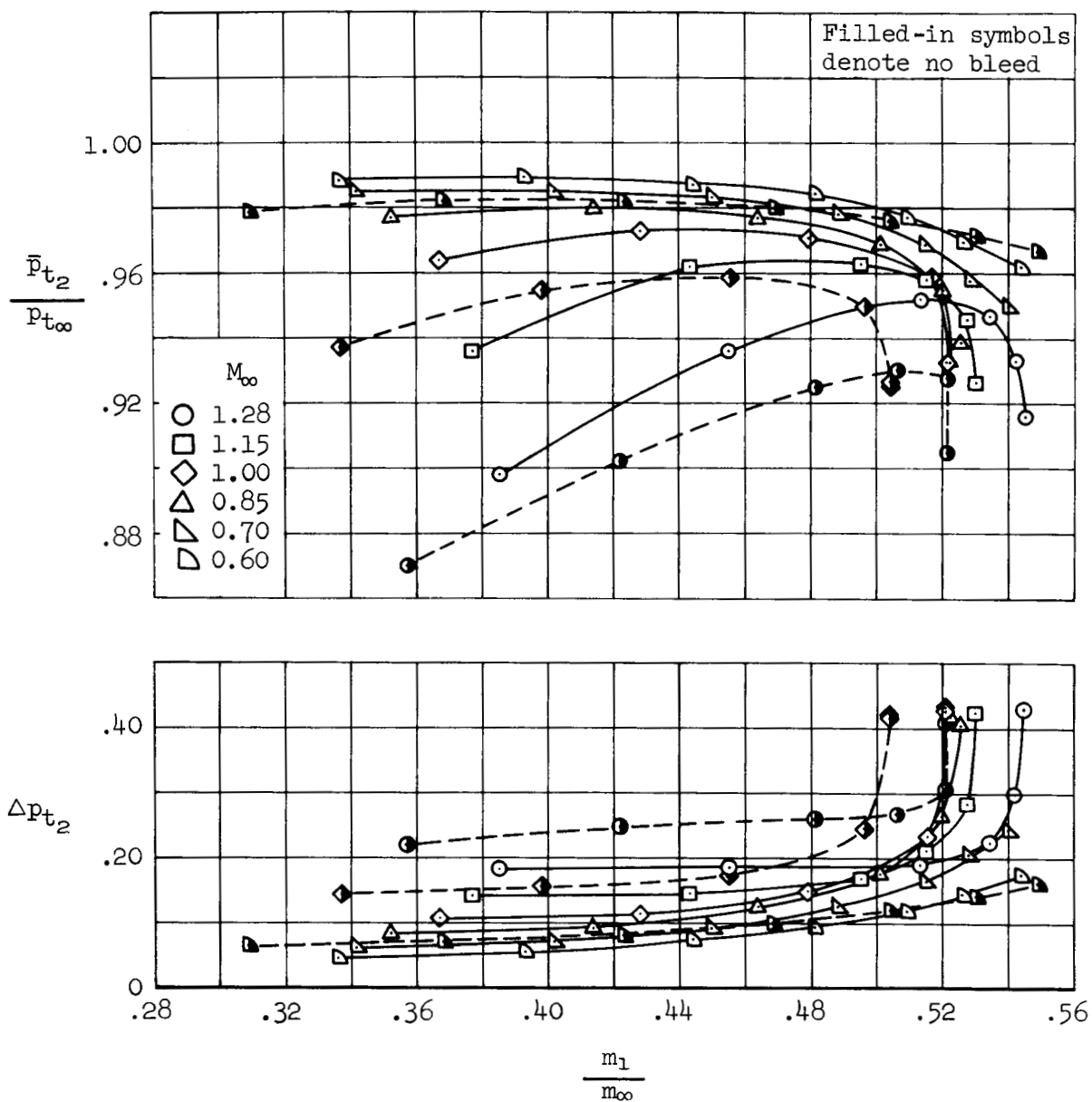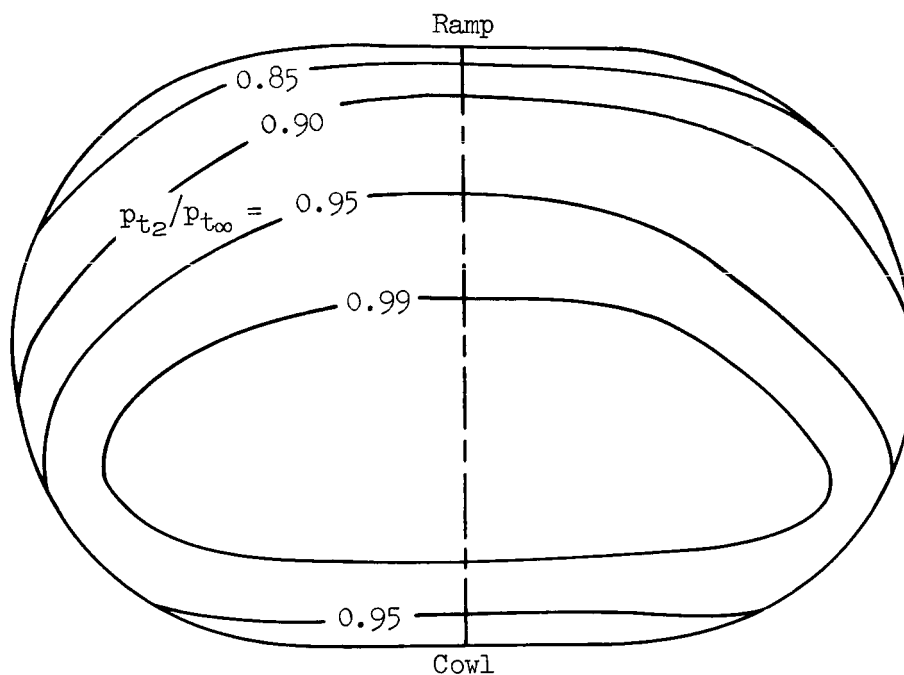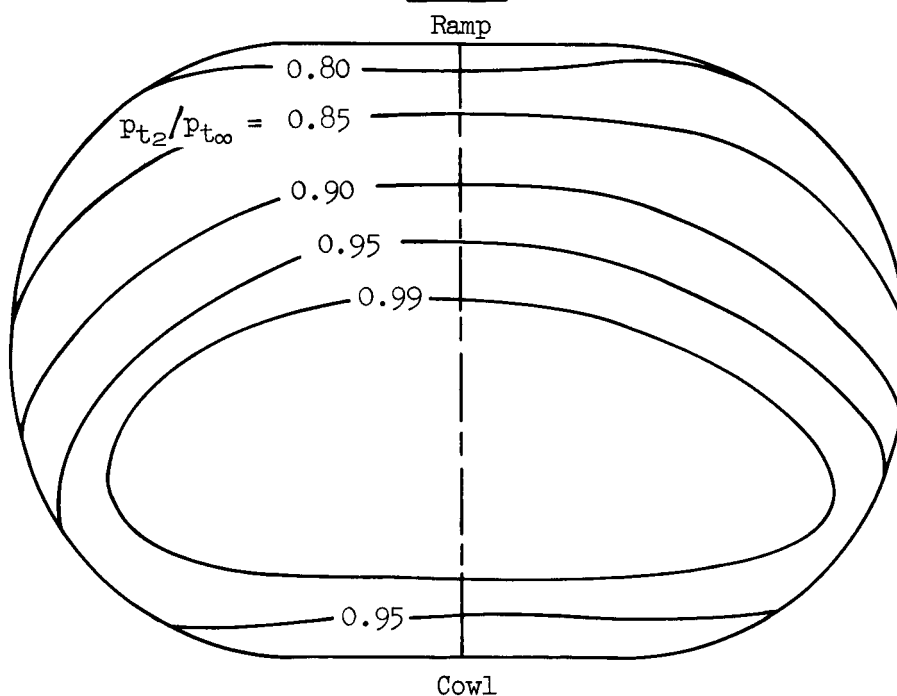Figure 5.- Details of the boundary-layer bleed system; $\delta_2 = 7°$, cowl fully retracted.

Figure 6.- Basic inlet performance at maximum throat height; $\delta_2 = 6°$, $\alpha = 0°$, $\beta = 0°$.

Ramp

0.85

0.90

$p_{t_2}/p_{t_\infty} = 0.95$

0.99

0.95

Cowl

$\bar{p}_{t_2}/p_{t_\infty} = 0.952$, $m_1/m_\infty = 0.513$, $\Delta p_{t_2} = 0.190$

<u>Bleed</u>

Ramp

0.80

$p_{t_2}/p_{t_\infty} = 0.85$

0.90

0.95

0.99

0.95

Cowl

$\bar{p}_{t_2}/p_{t_\infty} = 0.930$, $m_1/m_\infty = 0.506$, $\Delta p_{t_2} = 0.268$

<u>No bleed</u>

(a) Maximum recovery

Figure 7.- Engine-face total-pressure ratio contours at $M_\infty = 1.28$; $\delta_2 = 6°$, $\alpha = 0°$, $\beta = 0°$.

Ramp

$p_{t_2}/p_{t_\infty} = 0.85$

0.82

0.90

0.95

0.97

Cowl

$\bar{p}_{t_2}/p_{t_\infty} = 0.898, \quad m_1/m_\infty = 0.385, \quad \triangle p_{t_2} = 0.182$

Bleed

Ramp

0.79

0.80

$p_{t_2}/p_{t_\infty} = 0.85$

0.90

0.94

Cowl

$\bar{p}_{t_2}/p_{t_\infty} = 0.870, \quad m_1/m_\infty = 0.357, \quad \triangle p_{t_2} = 0.220$

No bleed
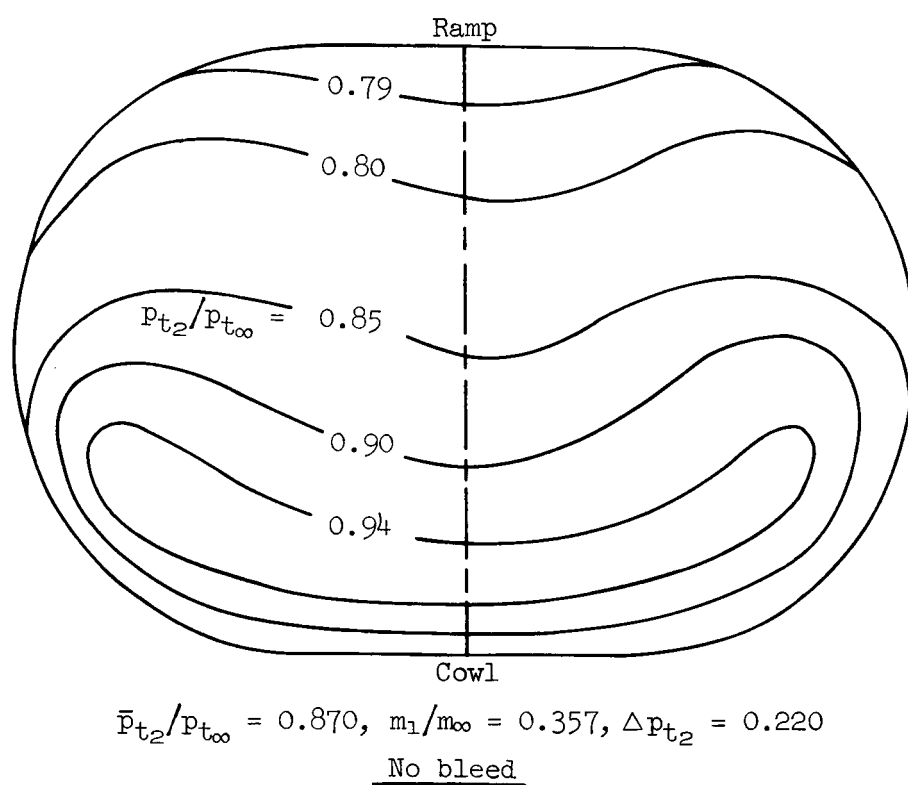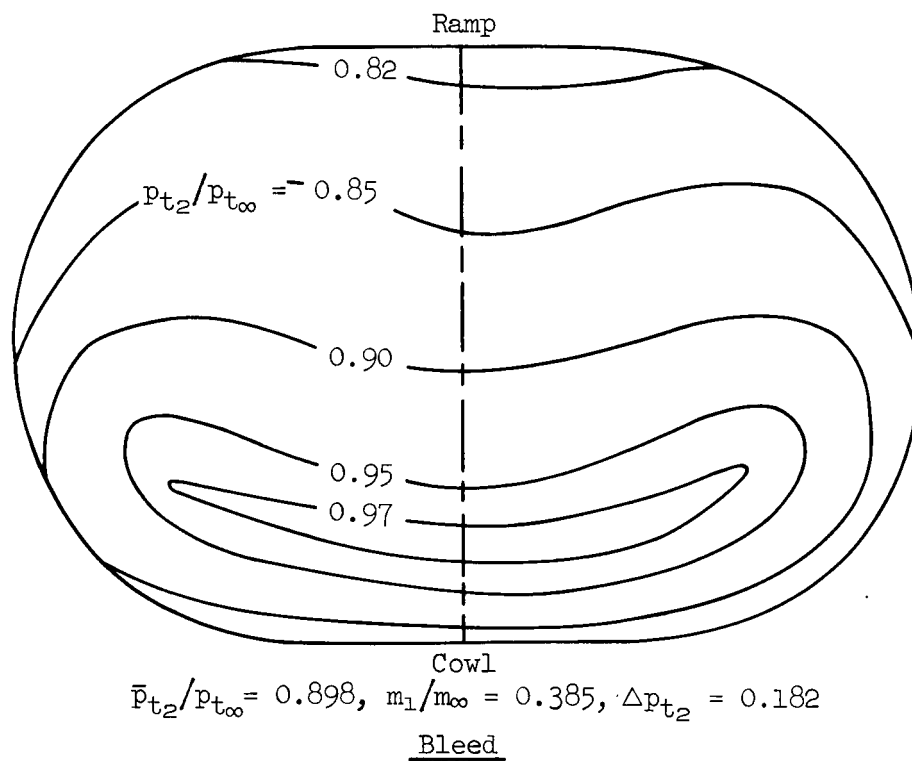
(b) Minimum recovery

Figure 7.- Concluded.
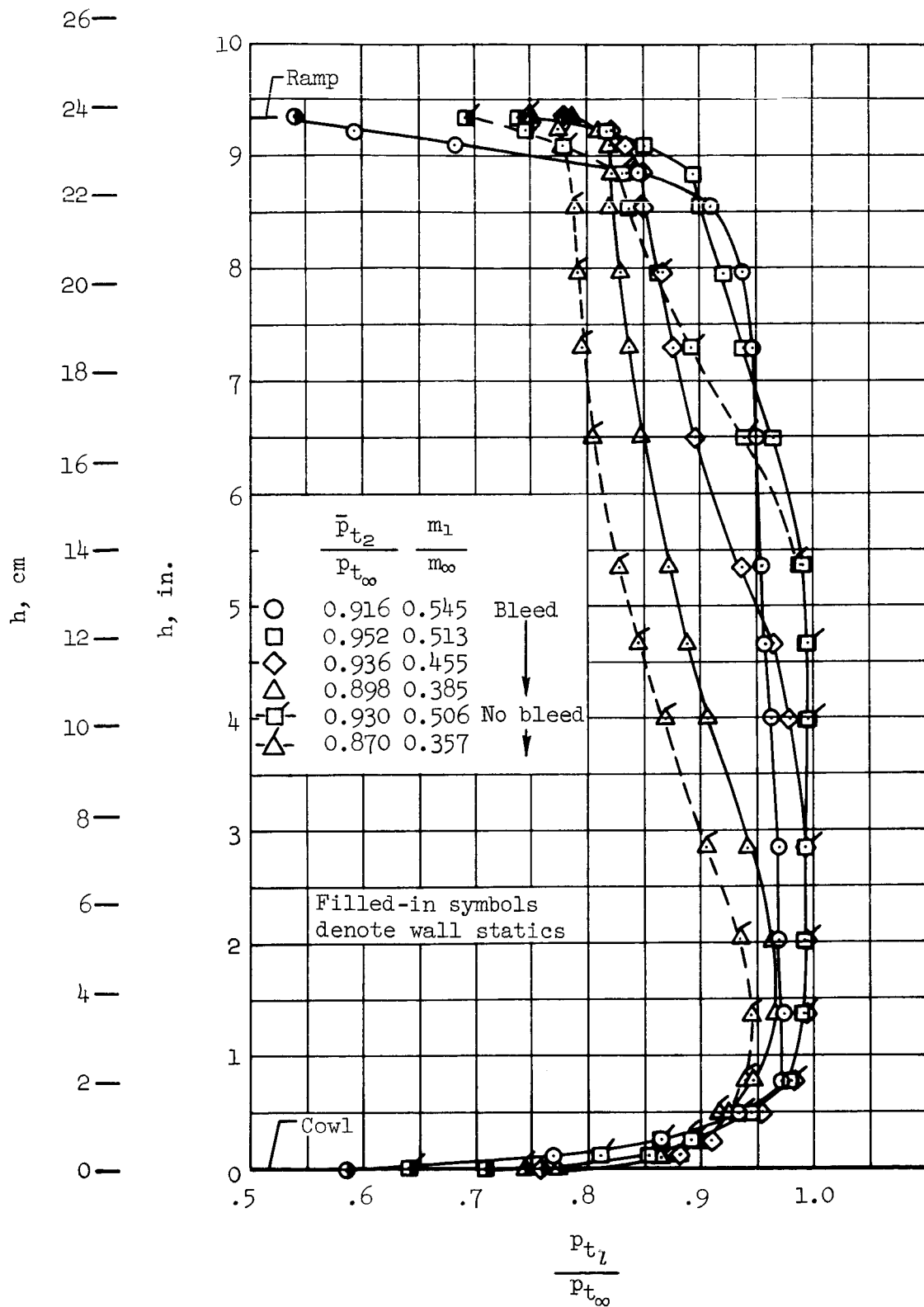
Figure 8.- Engine-face vertical total-pressure profiles at $M_\infty = 1.28$; $\delta_2 = 6°$, $\alpha = 0°$, $\beta = 0°$.
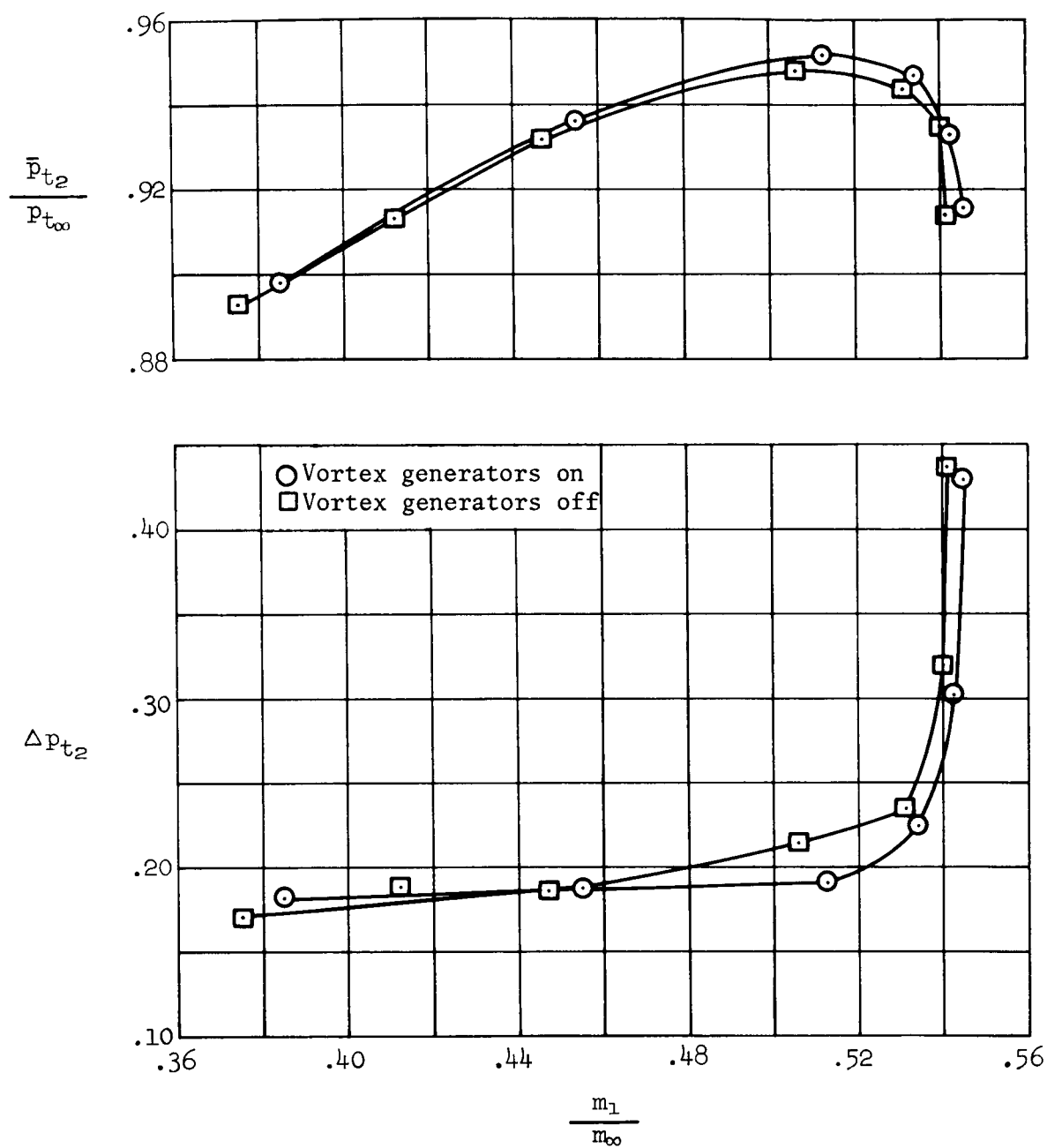
Figure 9.- Effect of vortex generators on inlet performance at $M_\infty = 1.28$; $\delta_2 = 6°$, $\alpha = 0°$, $\beta = 0°$.
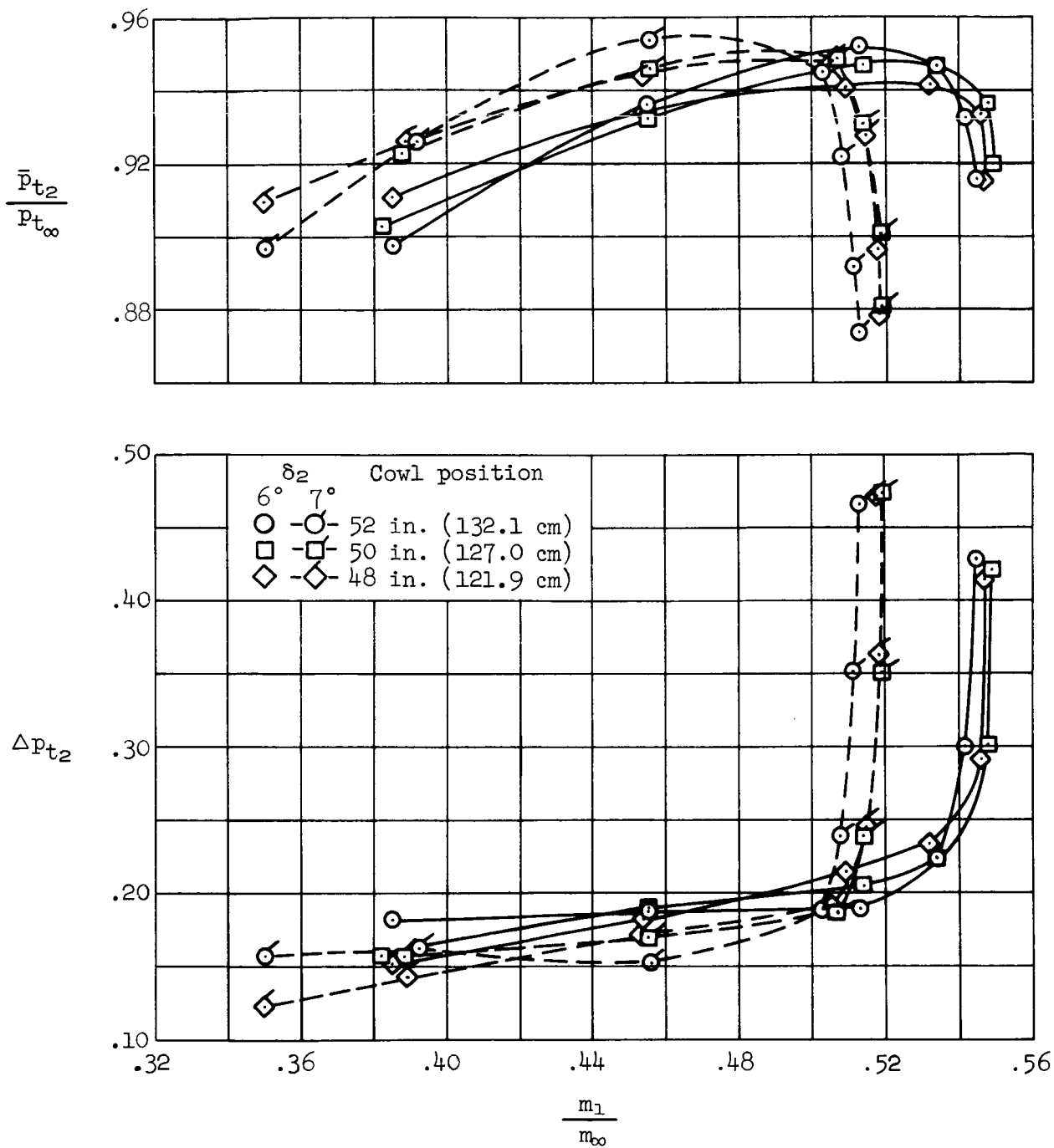
Figure 10.- Effect of cowl position and throat height on inlet performance at $M_\infty = 1.28$; $\alpha = 0°$, $\beta = 0°$.
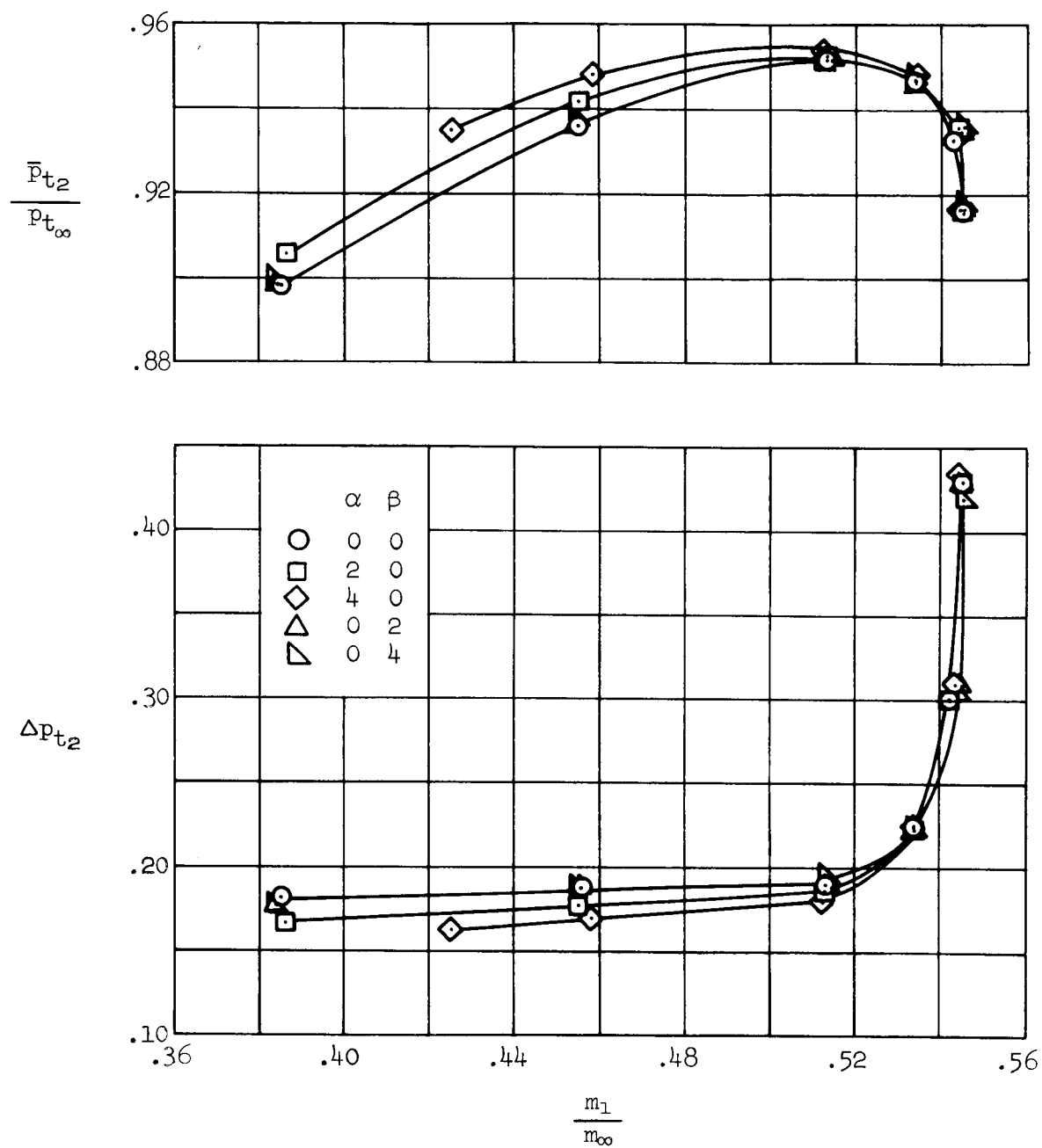
Figure 11.- Effect of angle of attack and yaw on inlet performance at $M_\infty = 1.28$; $\delta_2 = 6°$.
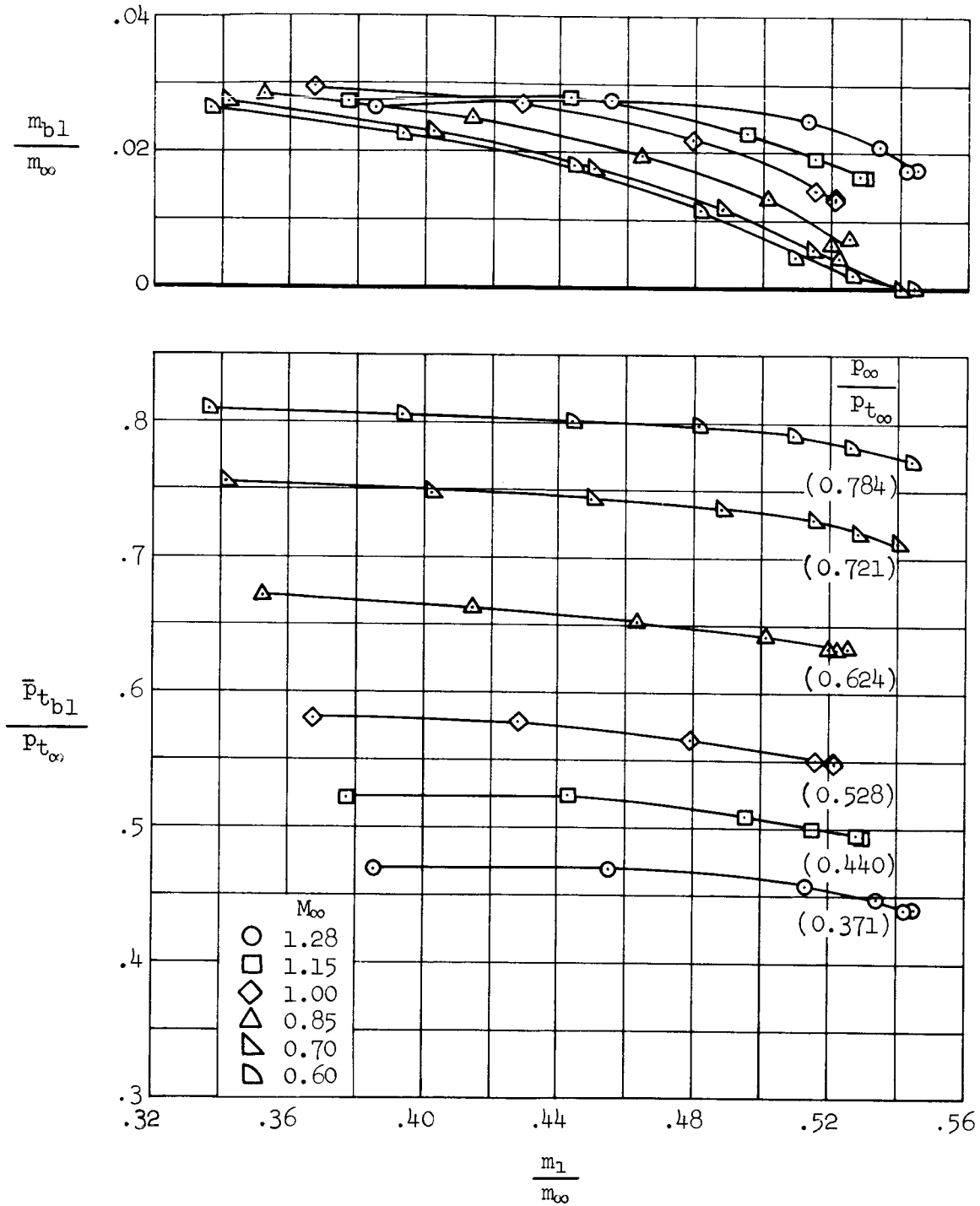
Figure 12.- Boundary-layer bleed mass-flow ratio and bleed-duct total-pressure recovery performance; $\delta_2 = 6°$, $\alpha = 0°$, $\beta = 0°$.
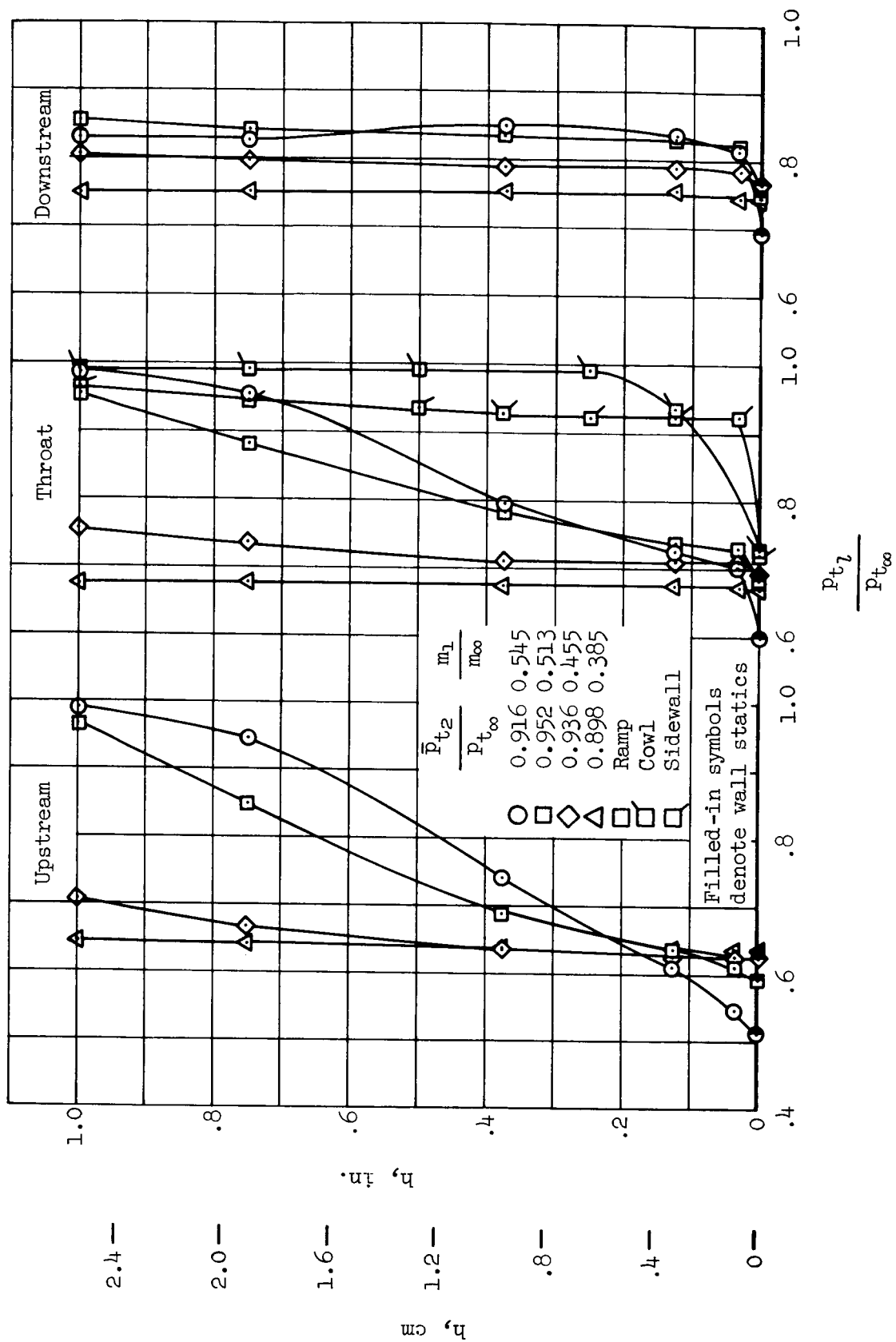
Figure 13.- Boundary-layer total pressure profiles at three duct stations; $\delta_2 = 6°$, $\alpha = 0°$, $\beta = 0°$.
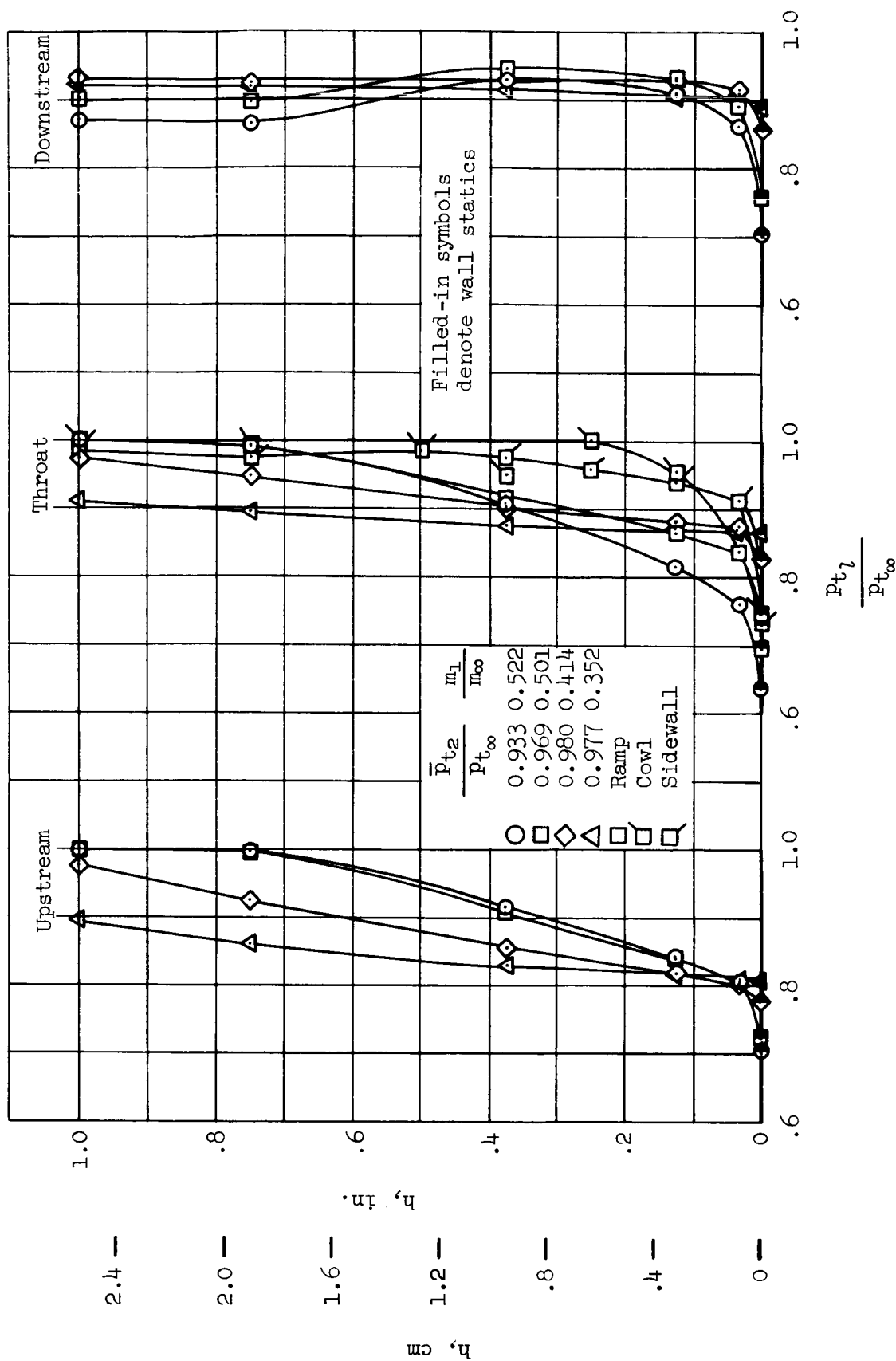
(a) $M_\infty = 1.28$.

(b) $M_\infty = 0.85$

Figure 13.- Concluded.
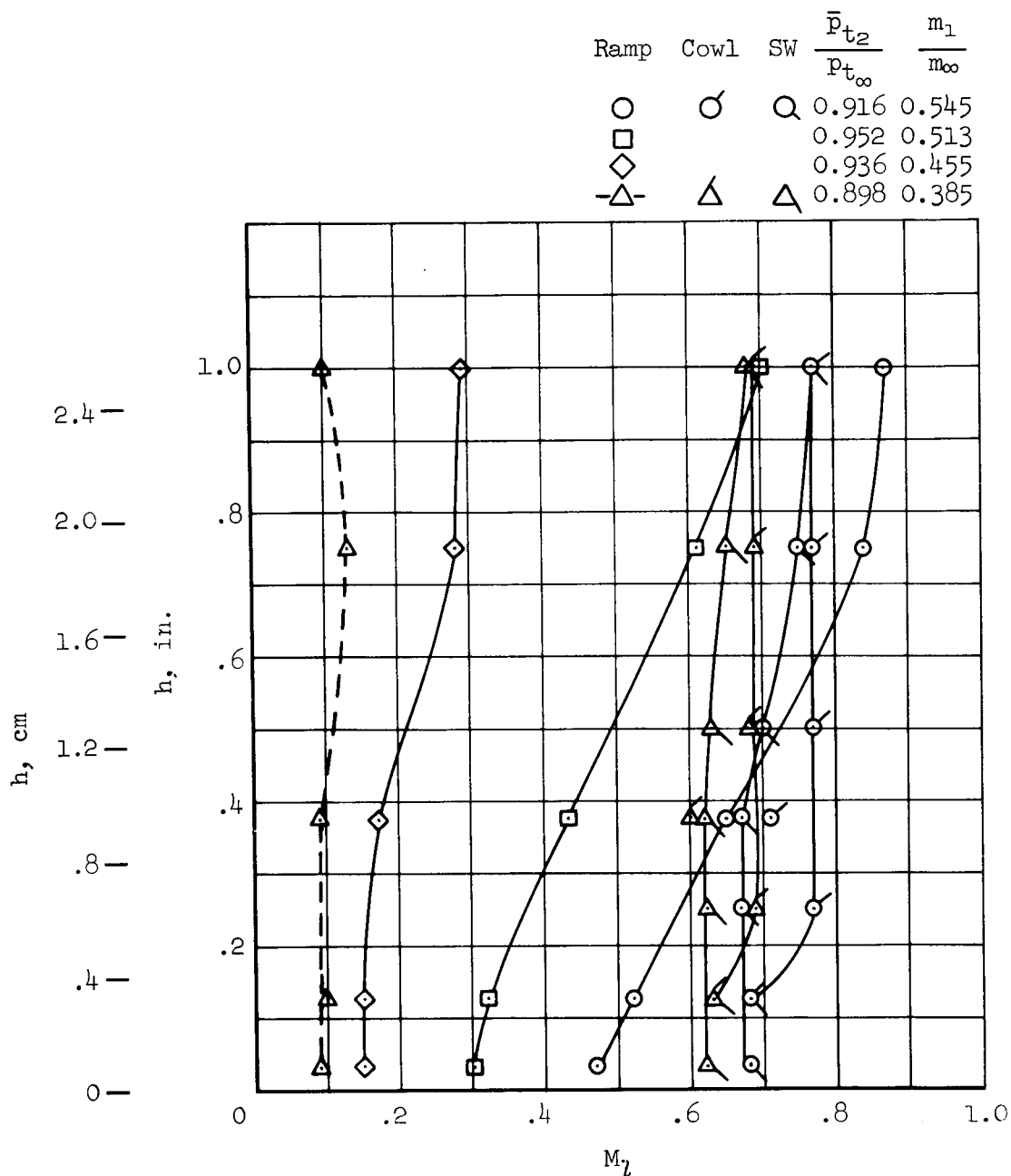
(a) $M_\infty = 1.28$

Figure 14.- Boundary-layer Mach number profiles at the throat station; $\delta_2 = 6°$, $\alpha = 0°$, $\beta = 0°$.
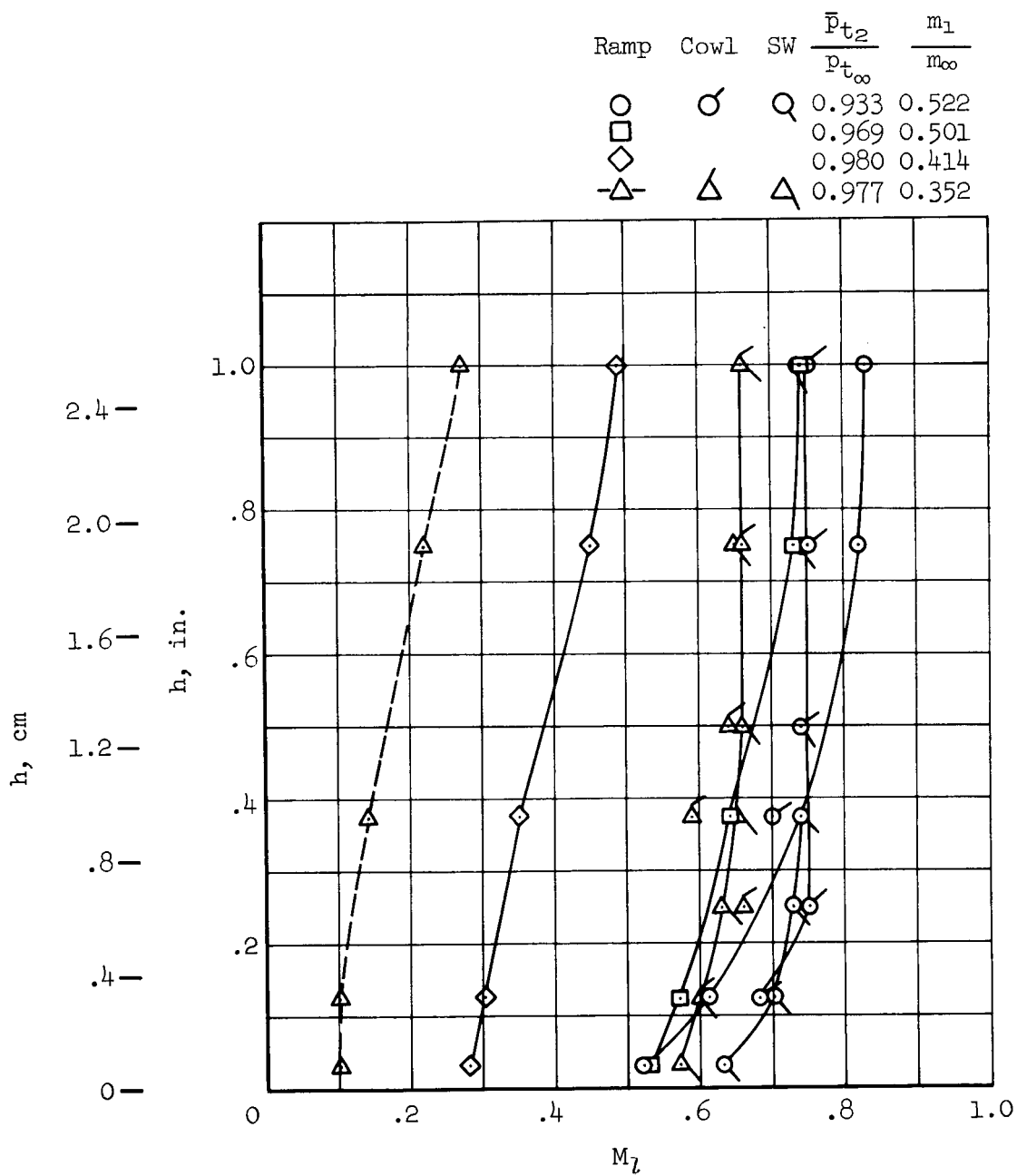
(b) $M_\infty = 0.85$

Figure 14.- Concluded.
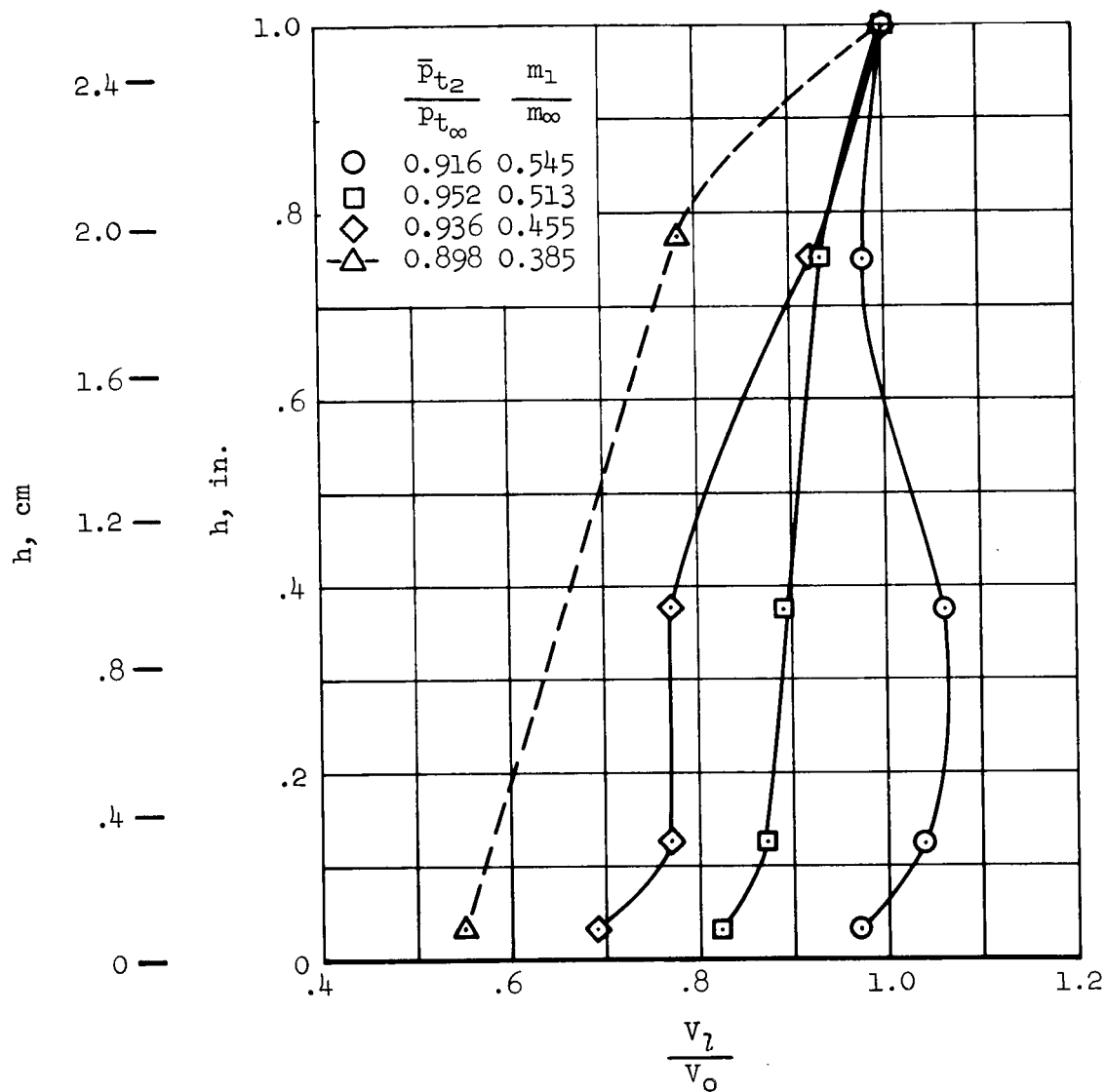
(a) $M_\infty = 1.28$

Figure 15.- Boundary-layer velocity profiles at the downstream ramp station; $\delta_2 = 6°$, $\alpha = 0°$, $\beta = 0°$.
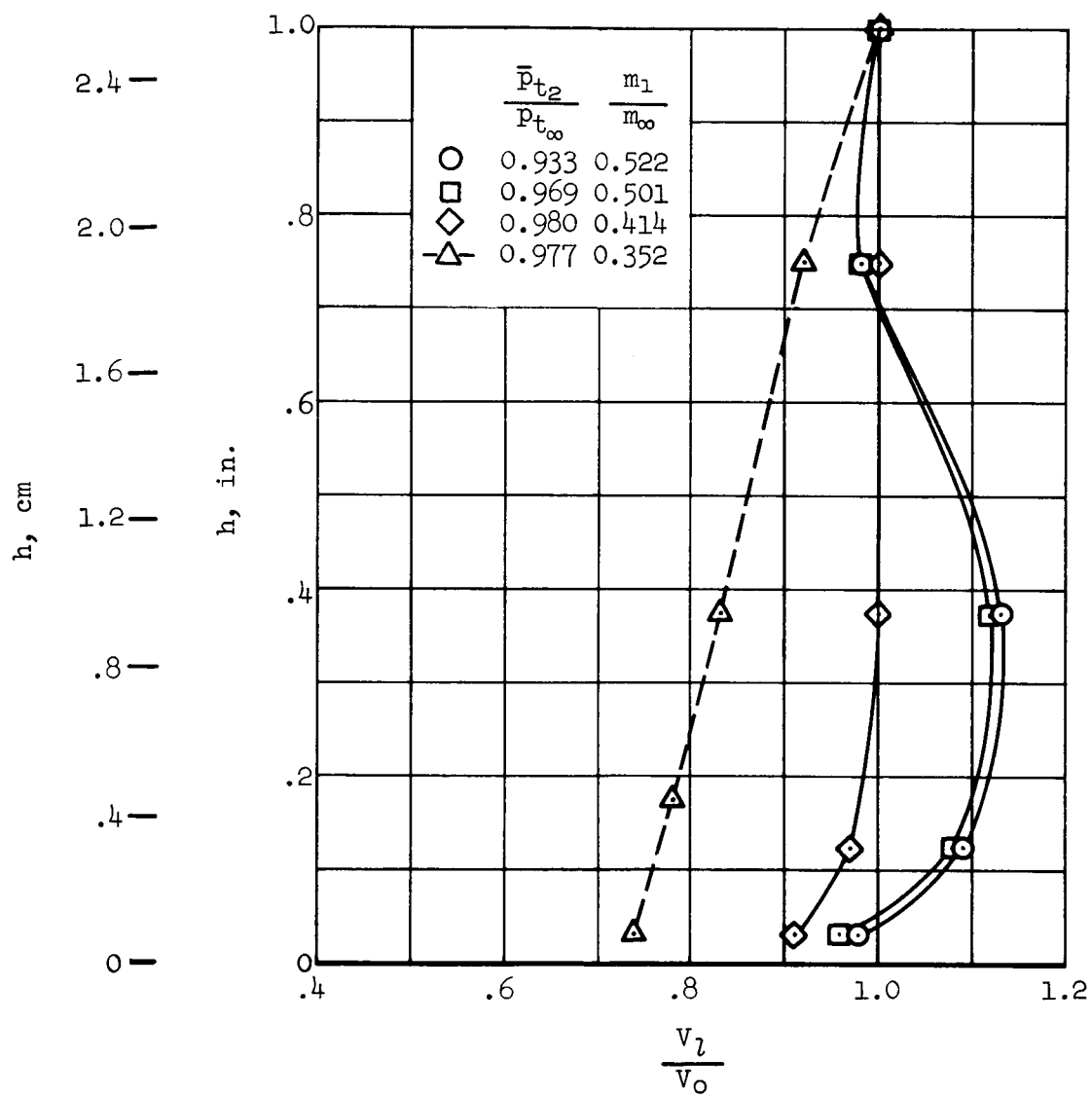
(b) $M_\infty = 0.85$

Figure 15.- Concluded.
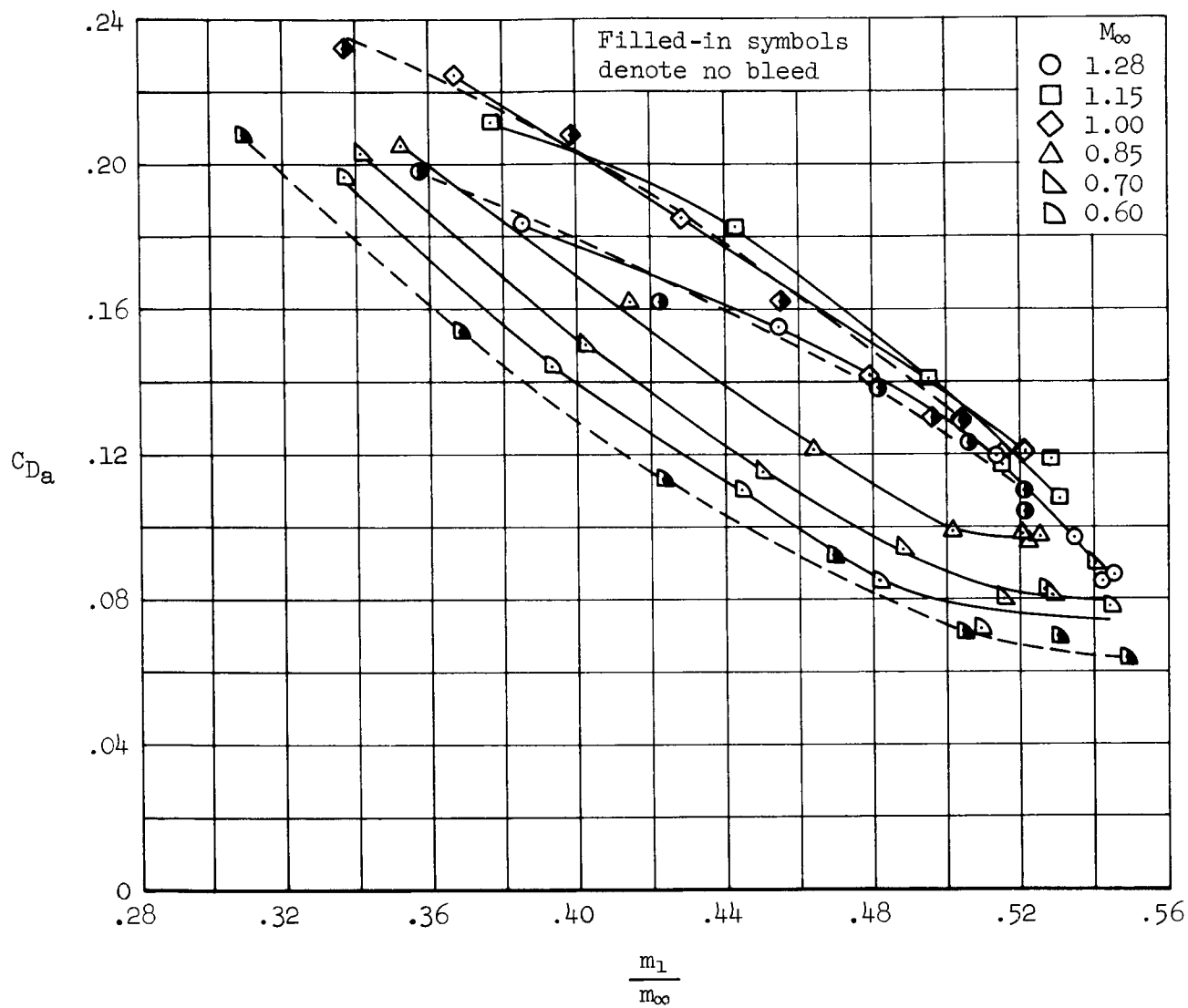
Figure 16.- Additive drag performance at maximum throat height; $\delta_2 = 6°$, $\alpha = 0°$, $\beta = 0°$.
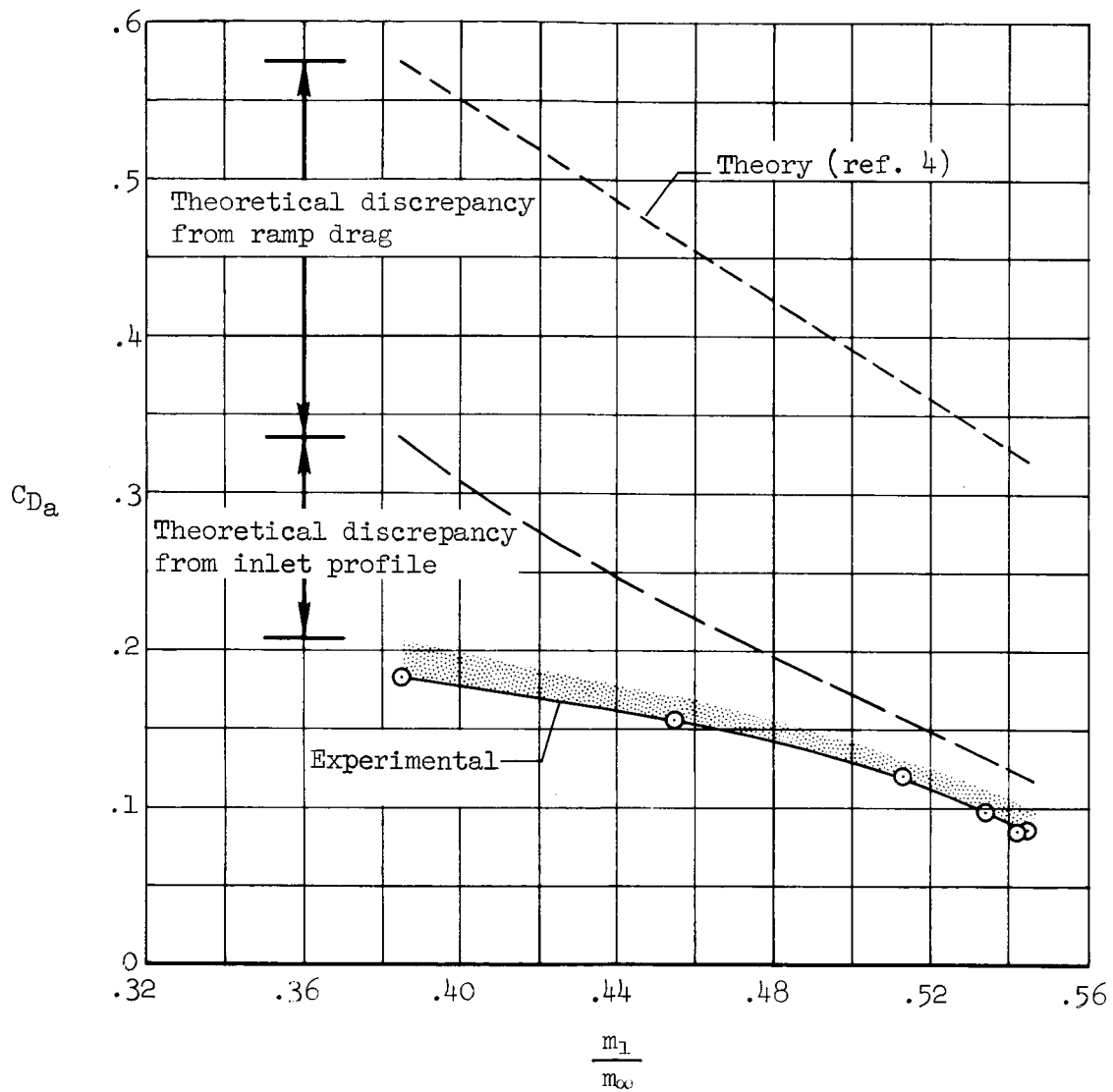
(a) $M_\infty = 1.28$

Figure 17.- Comparison of theoretical and experimental additive drag; $\delta_2 = 6°$, $\alpha = 0°$, $\beta = 0°$.
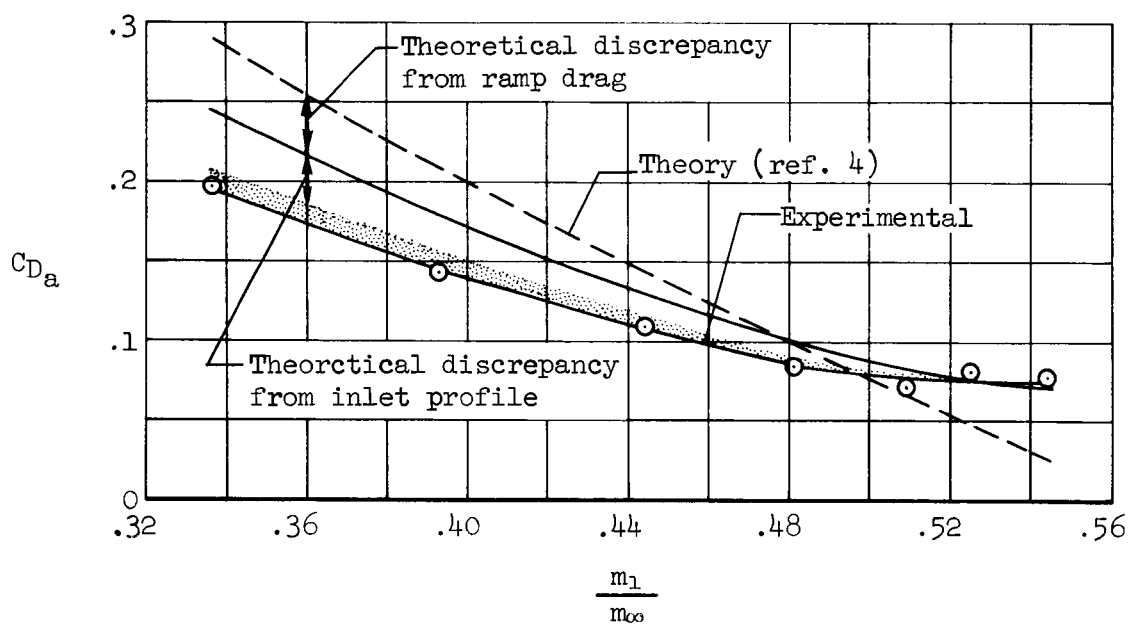
(b) $M_\infty = 0.60$

Figure 17.- Concluded.
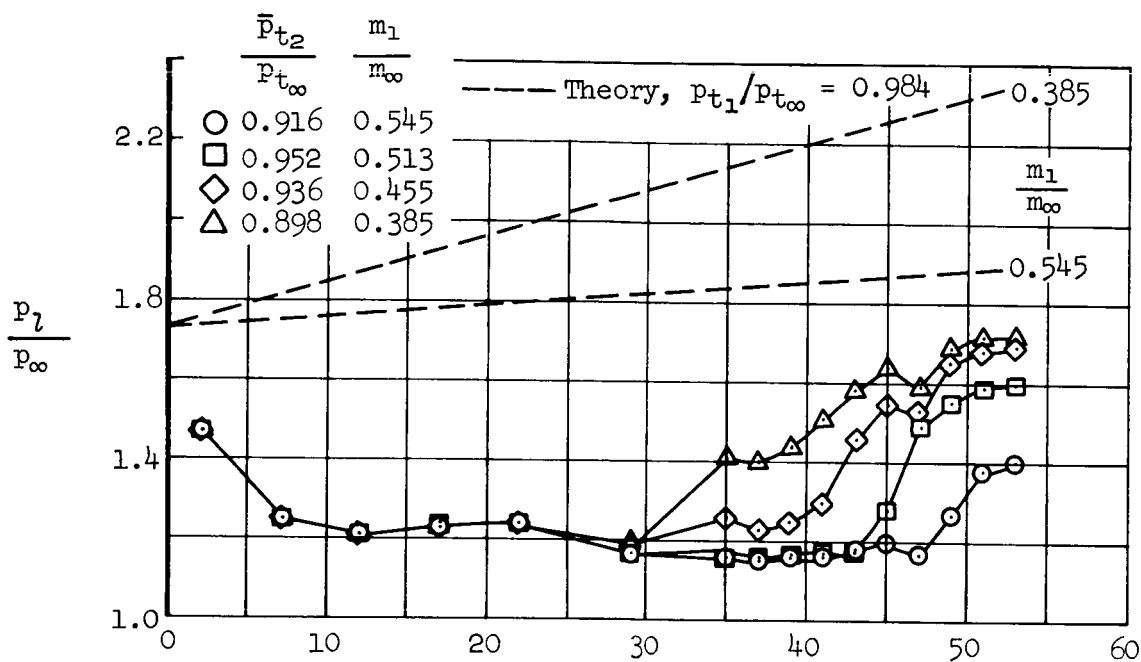
(a) $M_\infty = 1.28$
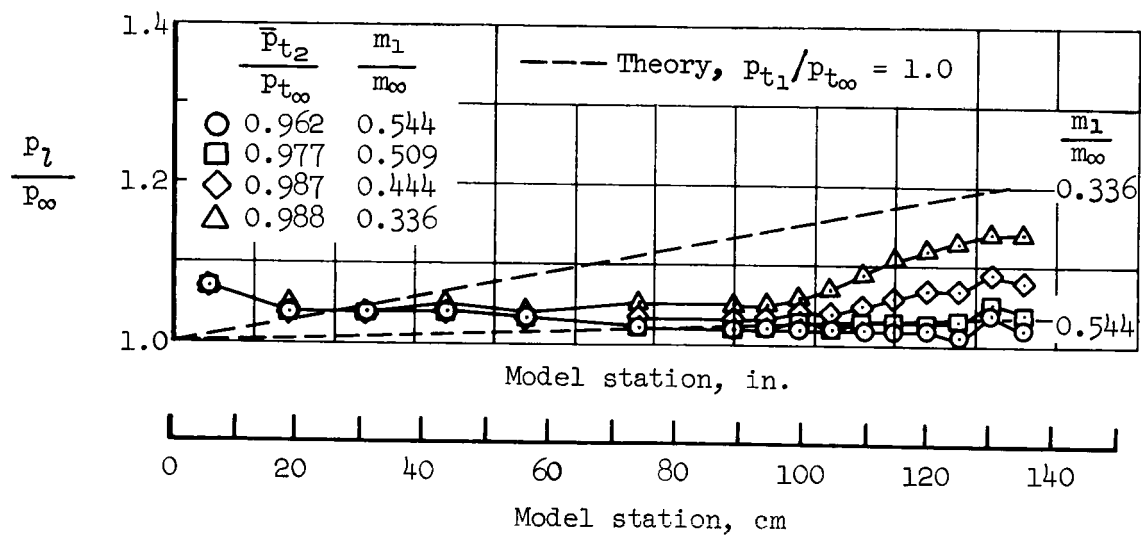
(b) $M_\infty = 0.60$

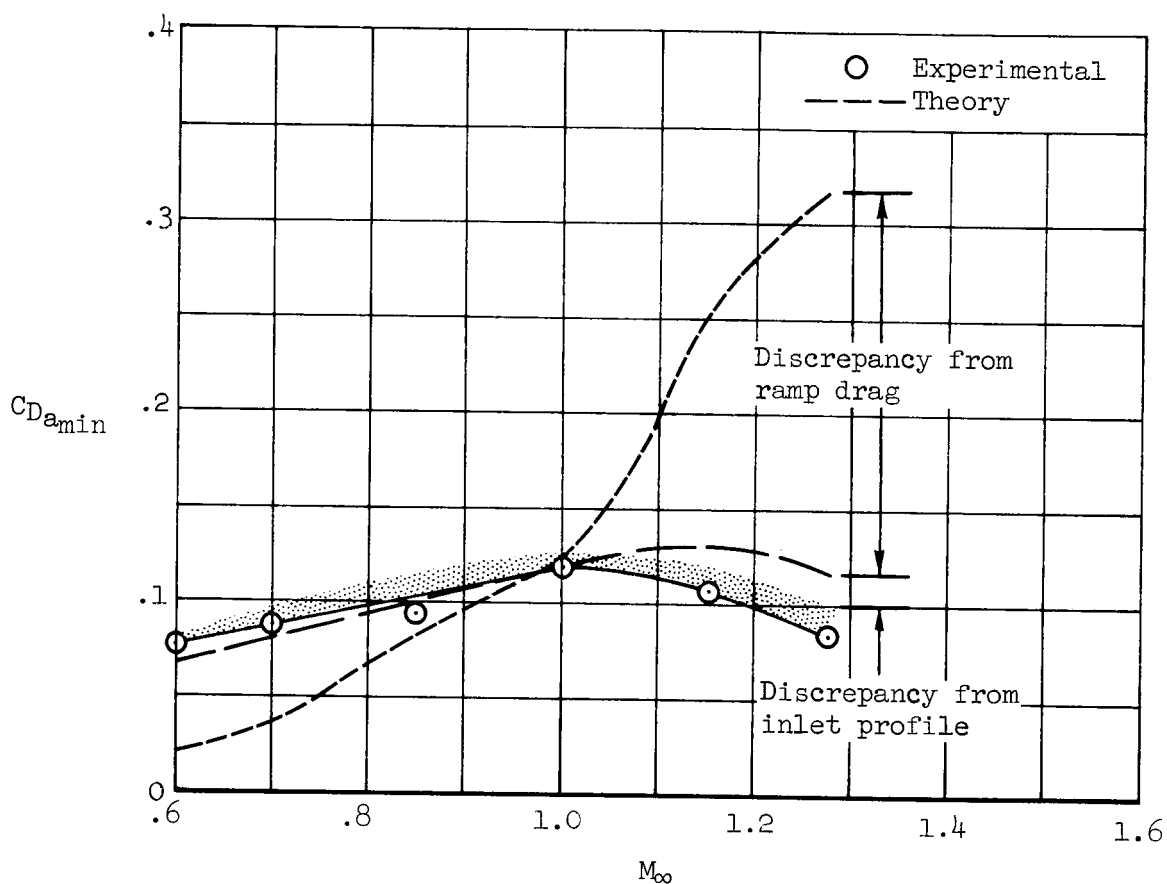Figure 18.- Static-pressure ratio distribution on the ramp surface; $\delta_2 = 6°$, $\alpha = 0°$, $\beta = 0°$.

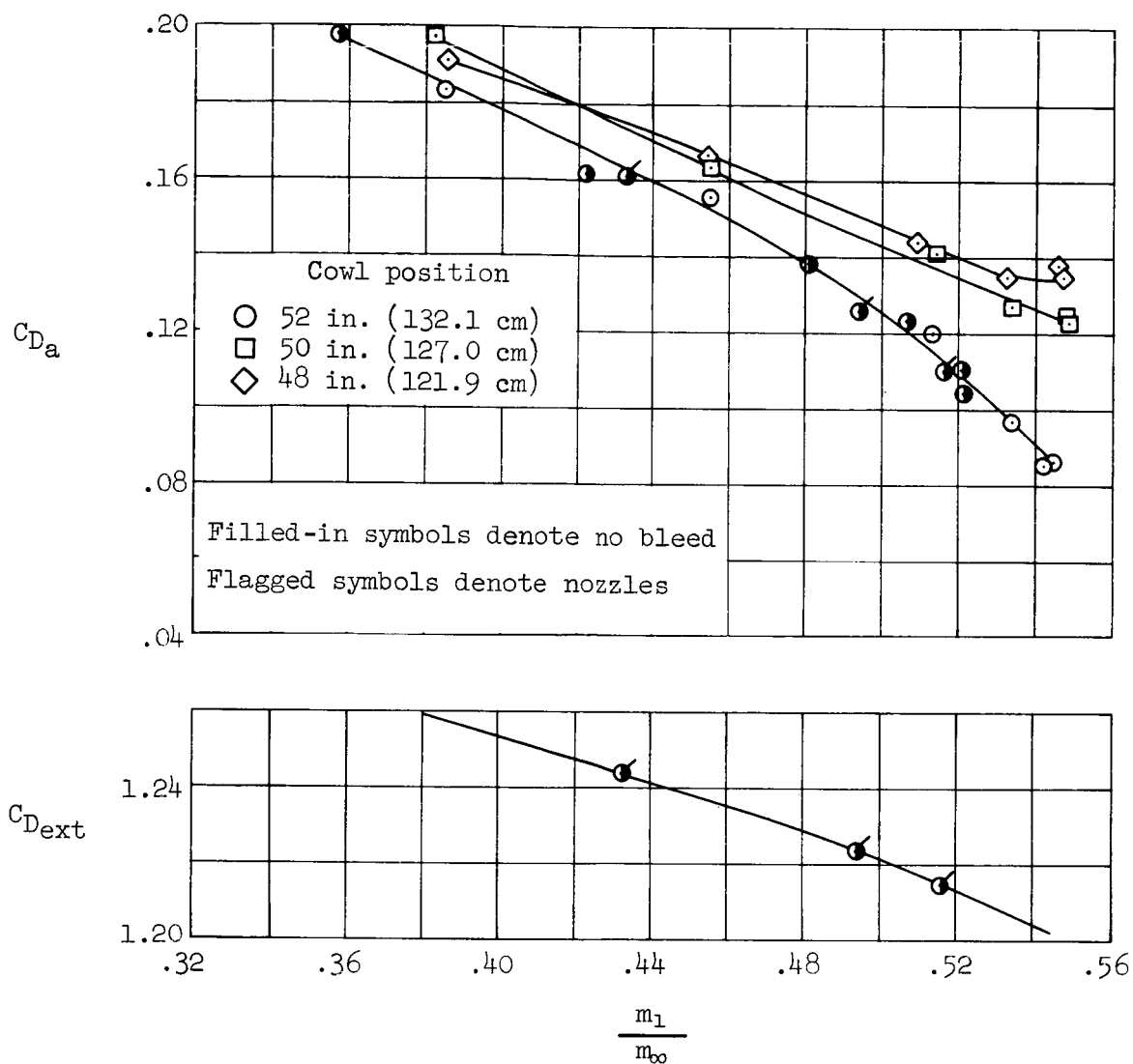Figure 19.- Comparison of theoretical and experimental minimum additive drag; $\delta_2 = 6°$, $\alpha = 0°$, $\beta = 0°$.

Figure 20.- Additive and external drag performance; $M_\infty = 1.28$, $\delta_2 = 6°$,
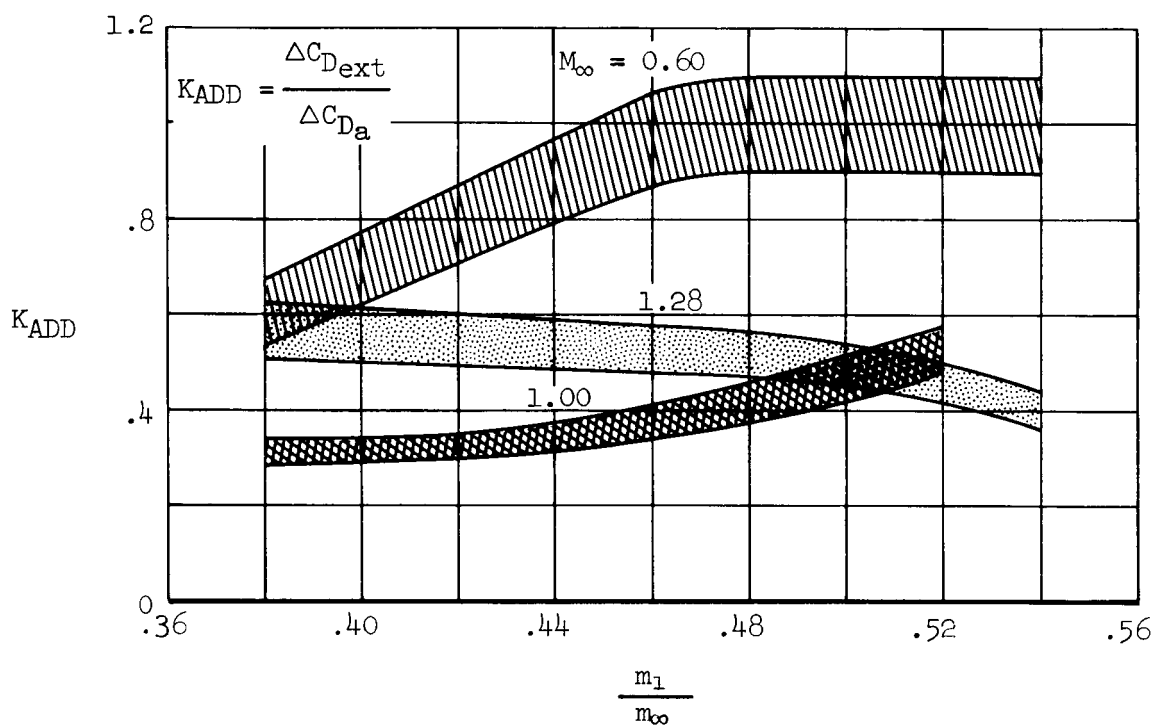$\alpha = 0°$, $\beta = 0°$.

Figure 21.- Variation of correction factor K_{ADD} with mass-flow ratio; $\delta_2 = 6°$, $\alpha = 0°$, $\beta = 0°$.